



Mapping the Interstellar Reddening and Extinction toward Baade’s Window Using Minimum Light Colors of ab-type RR Lyrae Stars: Revelations from the De-reddened Color–Magnitude Diagrams

Abhijit Saha¹ , A. Katherina Vivas² , Edward W. Olszewski³, Verne Smith¹, Knut Olsen¹ , Robert Blum^{1,4} , Francisco Valdes¹ , Jenna Claver¹, Annalisa Calamida^{1,5} , Alistair R. Walker² , Thomas Matheson¹ , Gautham Narayan^{1,5} , Monika Soraisam¹, Katia Cunha^{3,6}, T. Axelrod³ , Joshua S. Bloom⁷, S. Bradley Cenko^{8,9} , Brenda Frye³, Mario Juric¹⁰, Catherine Kaleida^{2,5}, Andrea Kunder^{2,11} , Adam Miller¹² , David Nidever¹, and Stephen Ridgway¹

¹ National Optical Astronomy Observatory, 950 N. Cherry Avenue, Tucson, AZ 85719, USA; saha@noao.edu

² Cerro Tololo Inter-American Observatory, National Optical Astronomy Observatory, Casilla 603, La Serena, Chile

³ Steward Observatory, The University of Arizona, Tucson, AZ 85721, USA

⁴ Large Synoptic Survey Telescope, 950 N. Cherry Avenue, Tucson, AZ 85719, USA

⁵ Space Telescope Science Institute, 3700 San Martin Drive, Baltimore, MD 21218, USA

⁶ Observatorio Nacional/MCTI, Rua Gen. Jose Cristino, 77 20921-400, Rio de Janeiro, Brazil

⁷ Department of Astronomy, University of California, Berkeley, CA 94720-3411, USA

⁸ NASA Goddard Space Flight Center, Mail Code 661, Greenbelt, MD 20771, USA

⁹ Joint Space-Science Institute, University of Maryland, College Park, MD 20742, USA

¹⁰ DIRAC Institute, Department of Astronomy, University of Washington, 3910 15th Avenue NE, Seattle, WA 98195, USA

¹¹ St. Martin’s University, 5000 Abbey Way SE, Lacey, WA 98503, USA

¹² Center for Interdisciplinary Exploration and Research in Astrophysics and Department of Physics and Astronomy, Northwestern University, 2145 Sheridan Road, Evanston, IL 60208, USA

Received 2019 January 29; revised 2019 February 13; accepted 2019 February 14; published 2019 March 19

Abstract

We have obtained repeated images of six fields toward the Galactic bulge in five passbands (u , g , r , i , z) with the DECam imager on the Blanco 4 m telescope at CTIO. From more than 1.6 billion individual photometric measurements in the field centered on Baade’s window, we have detected 4877 putative variable stars. A total of 474 of these have been confirmed as fundamental mode RR Lyrae stars, whose colors at minimum light yield line-of-sight reddening determinations, as well as a reddening law toward the Galactic Bulge, which differs significantly from the standard $R_V = 3.1$ formulation. Assuming that the stellar mix is invariant over the 3 square-degree field, we are able to derive a line-of-sight reddening map with sub-arcminute resolution, enabling us to obtain de-reddened and extinction corrected color–magnitude diagrams (CMDs) of this bulge field using up to 2.5 million well-measured stars. The corrected CMDs show unprecedented detail and expose sparsely populated sequences: for example, delineation of the very wide red giant branch, structure within the red giant clump, the full extent of the horizontal branch, and a surprising bright feature that is likely due to stars with ages younger than 1 Gyr. We use the RR Lyrae stars to trace the spatial structure of the ancient stars and find an exponential decline in density with Galactocentric distance. We discuss ways in which our data products can be used to explore the age and metallicity properties of the bulge, and how our larger list of all variables is useful for learning to interpret future LSST alerts.

Key words: Galaxy: bulge – Galaxy: stellar content – Galaxy: structure – ISM: dust, extinction – methods: data analysis – stars: variables: RR Lyrae

Supporting material: data behind figure, figure set, machine-readable tables

1. Introduction

Observationally the Galactic bulge is a concentration of stars toward the galactic center with chemistry, age distribution, and dynamics that set it apart from the disk and halo. A comprehensive review with leads into the extensive literature is given by Barbuy et al. (2018). By combining what we know about our bulge with those in other galaxies, we are led to understand that bulges come in two forms: classical bulges and pseudo-bulges (Kormendy & Kennicutt 2004). Modern observations of the Milky Way bulge indicate that it has a bar (Dwek et al. 1995) with some characteristics of a classical bulge and some of a pseudo-bulge. While the majority of Bulge stars seem to be old, there is still debate about the percentage of younger stars, a debate that can be informed by the inspection and analysis of color–magnitude diagrams (CMDs) from which (a) the line-of-sight reddening and extinction are removed, and

(b) contamination by foreground stars is identified and eliminated on the basis of proper motions.

Thus, in addition to the complications of performing accurate photometry in severely over-crowded fields, the construction of suitable CMDs involves removing reddening on the finest possible angular scales. The color of the red clump (RC) stars just off the giant branch has been used as a standard color marker (or standard crayon) in many studies, most notably by Nataf et al. (2013, 2016) and references therein. They found that not only does the standard reddening law predict the line-of-sight reddening to the bulge incorrectly, but that the true reddening law in these directions varies on angular scales of a few degrees.

Removal of foreground stars using proper motions up to 19th mag over wide fields of view is possible with *Gaia*, though we may have to wait for the mission to complete to do this comprehensively. It may well be that due to the high stellar

Table 1
Field Positions

Field Name	R.A. (J2000) (h:m:s)	Decl. (J2000) (° : ' : ")	Galactic Long. (degrees)	Galactic Lat. (degrees)
B1	18:03:34.0	-30:02:02	1.02	-3.92
B2	18:09:24.4	-31:26:06	0.40	-5.70
B3	18:26:41.9	-22:39:21	10.00	-5.00
B4	18:14:23.3	-27:56:49	4.00	-5.00
B5	18:26:41.8	-33:45:24	0.00	-10.00
B6	17:48:10.8	-37:08:15	353.25	-4.70

density in these areas, *Gaia*'s selection of stars in this part of the sky is incomplete. Over time, the VVV survey (Minniti et al. 2010) and its follow-up provide both the time base and object completeness, which are likely required to complete the task. From the analysis of AGB and cool supergiant stars near the Galactic center, Blum et al. (2003) implied that about 25% of the stars in the central few parsecs are younger than 5 Gyr. However, this may not be representative of the bulge as a whole. The *Hubble Space Telescope* (*HST*) has already been used to carry this out for small fields of view in the bulge (e.g., Clarkson et al. 2008; Calamida et al. 2014), with ensuing cleaned CMDs such as by Brown et al. (2009), and more recently by Bernard et al. (2018). The latter work goes on to derive star formation histories in different bulge fields from their CMDs and report that up to 20 or 25% of the most metal-rich stars are younger than 5 Gyr. The drawback is that rare(r) stars can only be seen as populations in larger-area studies than possible with *HST*, and reddening and extinction corrections used in these studies involve adopting the standard Galactic extinction law, which Nataf et al. (2013, 2016) show to be invalid.

In this paper we explore an alternative route to deriving reddening and extinction following the precepts enunciated by Sturch (1966) about the constancy and universality of the colors of fundamental mode RR Lyrae stars while they are in the pulsation phase corresponding to near minimum light. The potential advantage of this approach is that since RR Lyrae are also standard candles, they can be used to investigate not only the reddening, but also the ratio of total to selective extinction. In our experiment, we have obtained and analyzed multi-band, multi-epoch wide-field bulge images to construct light curves of the RR Lyraes and employ them to examine the intervening dust reddening and extinction. The emphasis is on avoiding any prior assumptions about the bulge's stellar population makeup.

RR Lyrae stars are also probes of ancient stellar populations, and their distribution in the bulge traces that of the oldest stars. Recent searches for these stars in the near-infrared through the very obscured inner regions of the bulge by the VVV survey (Minniti et al. 2010) indicate that these stars do not follow the bar-like structure, but have a smoother distribution (Minniti et al. 2017). This is contrary to an older result based on OGLE data (Pietrukowicz et al. 2012), who claim that the RR Lyrae spatial distribution is elongated along the Galactic bar. It is quite possible that the accuracy in the adopted reddening and total to selective reddening laws impact such findings.

We obtained images of six select fields toward the general direction of the Galactic center with the DECam imager (Flaugher et al. 2015) over multiple epochs in five different passbands, u , g , r , i , z . The chosen fields are shown in Table 1,

and named B1 through B6. B1 is centered on the well-known "Baade's Window" and gets close to the direction of the Galactic center while remaining relatively transparent. The footprint of the DECam field is significantly larger than the original area considered by Baade and has patches of reddening much higher than the value of $E(B - V) \sim 0.7$ often ascribed to it. Figure 1 shows an image of the field in the u passband, which highlights the patchiness in extinction that must be dealt with. B2 is an adjacent field midway between two fields found by Blanco (1992) and Blanco & Blanco (1997), with lower and less uneven extinction than B1, but slightly farther from the direction of the Galactic center. There is a small intentional overlap between B1 and B2 for the purpose of verifying photometric accuracy in our data. B5 is set $\sim 10^\circ$ south of the Galactic Center, and is intended as a probe of the region off the Galactic plane, but within the bulge. B3 and B4 are fields at similar Galactic latitude as B1, but $\sim 10^\circ$ and $\sim 5^\circ$ away in longitude, respectively, in the direction of the near side of the bar, while B6 is 10° away on the far side of the bar. These field choices sample the run of stellar populations along and across the Galactic disk. The exact placement of the fields was made to have minimal extinction compared to their surroundings using the dust maps by Schlegel et al. (1998).¹³ This paper deals only with field B1, but also details the analysis methodology that will be used for the remaining fields.

The organization of this paper is as follows. Section 2 describes the observations. Section 3 describes the processing of the data, including photometry and calibration onto an absolute flux based magnitude scale for the native DECam passbands. Section 4 deals with the detection of variable stars, follow-up analysis including period determination to identify the RR Lyrae stars, template light-curve fitting, measurement of minimum light brightness in each passband, and determination of completeness. Section 5 describes the derivation of reddening to the individual fundamental mode RR Lyrae stars, and utilization of the differential reddening and extinction of the ensemble of these stars to independently derive the total to selective absorption ratios for the line of sight encompassed by the field B1. We present a comparison with the standard extinction law. In Section 6 the observed colors and magnitudes of all stars in the field are used in conjunction with the RR Lyrae reddening values to correct the observed CMDs for extinction, and the prominent features in the corrected CMD are discussed. We show a reddening map in Section 7 with angular bins of 0.5×0.5 arcmin. The implications of our analysis of reddening for tracing the geometry of the Galactic bulge are presented in Section 8. In Section 9 we summarize our findings and suggest how the data set presented in this paper may be profitably used in future analyses and investigations.

An ancillary benefit of the data set is that we have light-curve data in many LSST-like passbands for a cornucopia of variable stars (and possibly transients) that begins to inform us about how to interpret the variability alert stream from LSST when it begins operation.

2. Observations

The journal of observations is given in Table 2. There were three dark runs in 2013, in May, June, and August, each of 3–4 nights. All six fields were visited three to four times on each of

¹³ <http://irsa.ipac.caltech.edu/applications/DUST/>

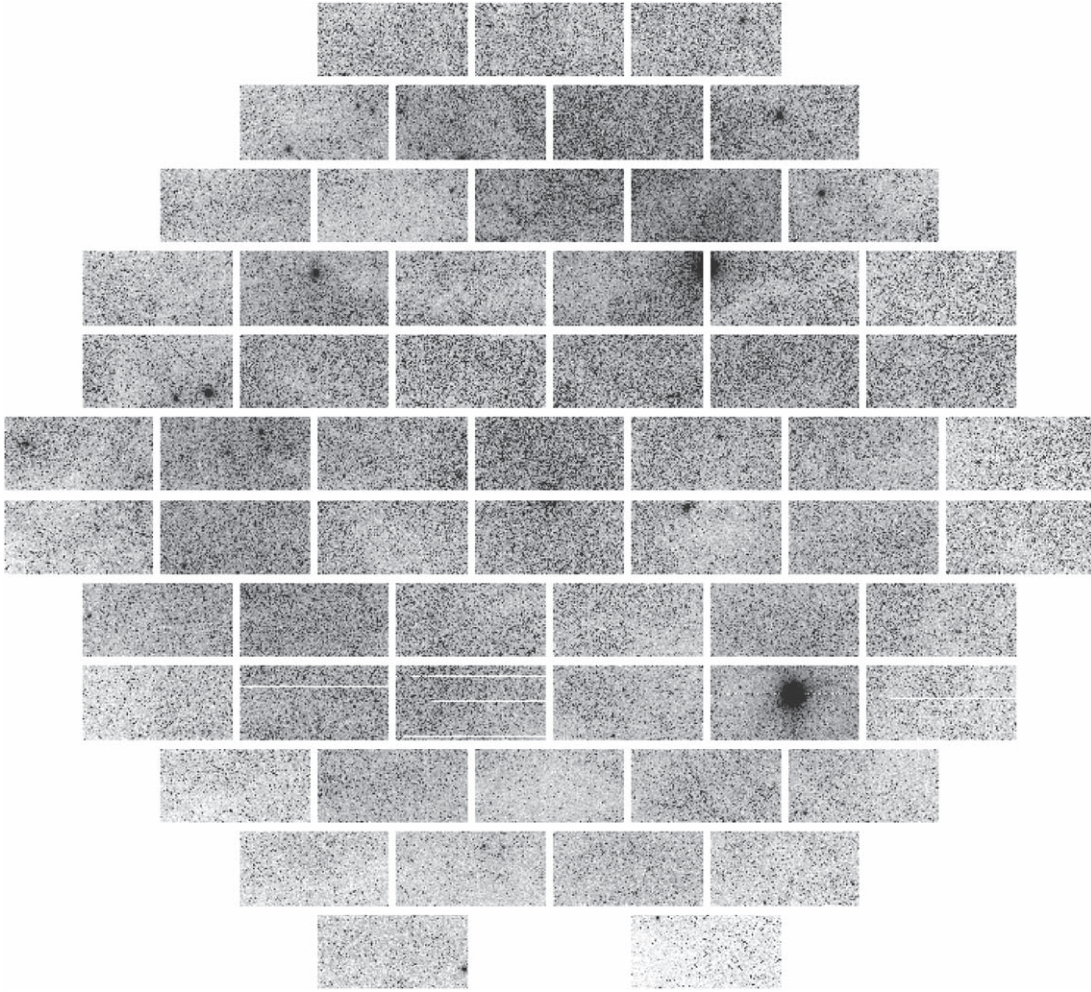


Figure 1. Panoramic image of the B1 field showing the full DECam field (with radius $\sim 1^\circ$) from a 300 s exposure in the u band. North is up, and east is to the left. The patchiness in extinction is apparent, with structure on scales of less than an arcminute (the individual chips have dimensions of 9×18 arcmin on the sky).

Table 2
Journal of Observations for Field B1 in all Bands

HJD-2,400,000.0	Passband	DECam Exposure No.	Exposure Time (s)
56423.659625	r	205418	100
56423.661128	i	205419	100
56423.662623	z	205420	100
56423.664117	g	205421	100
56423.665618	u	205422	300
56423.808243	r	205489	100
56423.809737	i	205490	100
56423.811255	z	205491	100
56423.812743	g	205492	100
56423.814222	u	205493	300

(This table is available in its entirety in machine-readable form.)

these nights (weather permitting), and exposed in all five bands u , g , r , i , z successively. Consecutive visits to the same field on any night were spaced about 2 hr apart. The exposure times (typically 300 s in u , 100 s in g , r , i , z) are long enough to detect F stars to $r \sim 24$ mag in dark skies and arcsec or better seeing in *uncrowded* fields in the absence of reddening/extinction. For these fields, and particularly for the B1 field, the crowding is

extreme and reddening is significant, so the actual detection limit is substantially brighter. In the best (and deepest) images, saturation sets in at $r \sim 15$ mag. Some of the images were taken in poorer seeing (up to 1.5 arcsec), and also on occasion through light clouds. Some additional epochs in the i , and z bands were obtained in 2013 June, during bright time. In addition, we obtained a set of much shorter exposures in 2015 March. These provide some measure of longer-term sampling of the brighter stars relative to the 2013 data, and also provide data for stars of interest that may have been inadvertently saturated in the longer exposures of 2013.

The images were processed through the NOAO DECam pipeline (Valdes et al. 2014), for bias and flat-field correction, bad pixel masking, and WCS (world coordinate system) fitting. Reduced images are available publicly through the NOAO Science Archive.¹⁴ We intend to make catalog data available through the Community NOAO Data Lab.¹⁵

3. Photometry, Cross-matching, and Calibration

We measured photometry in these very crowded fields using a variant of the DoPHOT program (Schechter et al. 1993)

¹⁴ <https://archive.noao.edu>

¹⁵ <https://datalab.noao.edu>

maintained by one of us (Saha). The procedures and considerations for optimizing the DoPHOT parameters and evaluating aperture corrections done using a bespoke procedure written in IDL are fully described in Section 3.2 of Saha et al. (2010) and need not be repeated here. The only differences, mentioned also in Vivas et al. (2017), are that unlike as in Saha et al. (2010), where the eight individual chips were combined into a single image by applying a gnomonic projection, in the present case the individual chips were processed independently, and the output photometry lists from the individual chips are concatenated into one single file for the whole image. The requirement for this is that the photometry across all chips (for a given image) be on the same footing. The justification for this premise has been previously given in Section 2 of Vivas et al. (2017).

We thus created independent photometry lists for each image. In addition to the aperture corrected instrumental magnitudes and associated error estimates, each object carries its R.A. and decl. positions, as well as the chip on which it was detected, and the pixel coordinates within that chip for each image/epoch, and the fitted background or “sky.” Each object on each image also carries the object type code assigned by DoPHOT. These codes distinguish well-fitted bona-fide single stars (type 1), multiple star blends (type 3), other extended objects (type 2), cosmic rays (type 8), image pathologies (types 4, 5, 8, and 9), and objects too faint to disambiguate between stars and extended objects or blends (type 7). In addition, the following attributes were also evaluated and recorded (for each object on each image):

1. Whether the object lies within 50 pixels of the chip’s edge
2. Whether there were two or more cosmic rays (or other pathologies) detected within a radial distance of 1 full width at half-maximum (FWHM) of the stellar point-spread-function (PSF) as measured along the major-axis of the PSF
3. Whether there were any bona-fide objects detected within a 1 FWHM radius footprint around the object as described previously and, if so, the cumulative flux from those objects expressed in magnitudes relative to the flux of the object in question. We denote this by $m_{\text{neighbors}}$
4. High and low percentile values for the distribution of fitted sky values of all objects for the entire image were also evaluated and recorded for each image
5. For all stellar objects on a given image, the total reported error for individual objects was fitted as a function of reported magnitude. The fitted value err_{exp} at a given measured brightness is a good expectation of what the measurement error should be for an object of that measured brightness. Reported errors much higher than the expected value for that brightness are suspect. The value $\text{err}_{\text{lim}} = 2 \times \text{err}_{\text{exp}} + 0.05$ for each object for each epoch was evaluated and recorded as an attribute.

The photometry list from the best deep image (best seeing in photometric conditions) in each passband was assigned as the deep template object list in that band, and a similarly suitable short exposure image in each band was assigned as the shallow template object list. For each band, the deep and shallow template lists were merged by matching to a coordinate tolerance of $0''.3$ (eliminating all multiple matches within this matching tolerance). The instrumental magnitude difference of

the matched objects was used to adjust the instrumental mag system of the shallow template to that of the deep one. This process allows the objects saturated in the deep template to be represented in the eventual object list in each passband, and at this point there is a “grand” template list in each of the five passbands that spans the full dynamic range of magnitudes spanned by both the deepest as well as shallow exposures, with instrumental mags on the system of the deep template. Finally, the r band “grand” template was adopted as the *master* template, containing the master list of all objects. In the subsequent processing, the numerical IDs of objects on this master list serve as the final object IDs for all objects in this field. Any objects that are not on this list (for whatever reason) are not considered further.

A particular detail for preparing the template lists before matching and combining into the “grand” templates is worth mentioning. Since the aperture corrections to go from fitted PSF mags to instrumental mags for each image were calculated independently for each chip, the zero-point in any chip can scatter about the mean for that image by a few hundredths of a mag (or in pathological cases by worse amounts). To mitigate this problem for the template images (to which all photometry calibration is eventually referred), they were compared against other images of similar depth (deep to deep and shallow to shallow) obtained in photometric conditions. Let m_{0j}^k be the measured aperture corrected magnitude of star j on image 0 (template) and on chip k . Let the same star as measured on image i and also on chip k be designated by m_{ij}^k , where image i was also in photometric conditions. If we selected only those j for which the reported measurement errors are small, and for which DoPHOT has reported that the object has an unambiguously stellar PSF, we can construct

$$\delta_i^k = \sum_j (m_{ij}^k - m_{0j}^k) / N \quad (1)$$

and

$$\Delta_i = \sum_k \delta_i^k / M, \quad (2)$$

where N is the total number of selected stars (over index j) in chip k being compared, and M is the number of chips (over index k). Δ_i is the overall offset between the instrumental mags of image i relative to the template image, and because it is an average over ~ 60 chips, it is essentially unaffected by small random errors in evaluating the zero-points on individual chips. The offset Δ_i can be caused by differences in atmospheric extinction (different airmass), and over longer durations by differences in system response and transmission. Consider the chip-to-chip fluctuation about this mean difference:

$$\epsilon_i^k = \delta_i^k - \Delta_i, \quad (3)$$

which shows the aggregate result of individual chip-to-chip aperture correction errors for both images i and 0.

If we have n images against which such a comparison can be made for the template, we can calculate the ensemble average like quantity C^k from the ϵ_i^k ’s:

$$C^k = \sum_{i=1}^n \epsilon_i^k / (n + 1), \quad (4)$$

which is a robust estimate of the correction to be added to the instrumental magnitudes for the template frame for each chip k .

All of the photometry lists in each passband were then matched one by one to the “grand” template for that passband, from which the offsets in the instrumental magnitudes relative to the “grand template” magnitudes were calculated on a chip-by-chip basis. All instrumental mags for the individual epochs were adjusted (single additive magnitude offset per chip) to put all the instrumental mags for all epochs on the scale of the “grand” template. The lists with the instrumental mags thus normalized were then matched individually to the master template (same as the r band “grand” template), and the object IDs from the master list were then attached to the matched objects in each object list for each epoch and for each passband. With this labeling, the measurements for any object can be extracted for any epoch and passband, along with all of the associated information discussed previously. The instrumental photometry for every epoch is normalized to that in the respective “grand” template for the relevant passband. Henceforth, all variability analyses can be carried out using either these normalized instrumental mags or using the calibrated AB-magnitudes described later. Calibration to any system of magnitudes requires only the determination of zero-points for the “grand” template of the respective passbands, the details of which are provided in the following paragraph. The normalized instrumental and object-labeled photometry for each epoch of each passband were then stored in a MySQL database, providing convenient access for subsequent variability analyses. There are 9,623,873 distinct objects in the database, each with multiple measurements at different epochs and different passbands (not all objects have all epochs in all passbands). They are labeled by an object ID corresponding to the running ID of the object on the master template. In all, the database for B1 measurements contains more than 1.6×10^9 individual photometric measurements. The above procedure ensures that all photometric measurements are placed on the same uniform instrumental system, independently in each of the passbands. Comparison of these instrumental magnitudes for high signal-to-noise ratio (S/N) objects across different exposures show that the self-consistency in the instrumental magnitudes is better than 0.02 mag rms.

On photometric nights, two of the newly calibrated DA white dwarf standards from Narayan et al. (2016) were also observed through a range of air-masses. These stars have calibrated spectral energy distributions, from which their true AB-magnitudes were calculated according to the prescription of Fukugita et al. (1996) for each of the five passbands. We then derived photometric solutions relating instrumental mags to AB-mags. In the u , g , r , i bands, photometric solutions have residuals with ~ 0.01 mag rms scatter. In the z band, which encompasses telluric water bands that can vary on timescales of minutes, as well as with position, the scatter is ~ 0.02 to 0.03 mag.

When these solutions are applied to the photometry of the “grand” templates (one for each passband), we obtain calibrated AB-mags for the native DECam passbands. This is the same system used in Vivas et al. (2017), where the luminosity and color relations for RR Lyraes are derived for precisely this system of magnitudes, making their results directly applicable to the data for the B1 field. Combining the scatter in the self-consistency in instrumental magnitudes discussed previously, and the total calibration accuracy, we estimate that the systematic uncertainty in the calibration of any exposure is thus ≈ 0.02 mag rms in u , g , r , and i , and

≈ 0.035 mag in z . Measurement errors for any object on any exposure are additional and are estimated by the measurement procedures, including by the DoPHOT program.

It should be pointed out that the analysis presented in this paper does not depend on what system of magnitudes we adopt, as long as the same system is used for all targets, including the globular cluster Messier 5 (NGC 5904), hereafter M5, where the color properties of the RR Lyrae stars are derived.

4. Variability Analysis

4.1. An Independent Identification of Variable Sources

Each object was tested for variability independently in each passband. However, a variability test is only meaningful if there are sufficient number of measurements of adequate quality. It is important to remove reported observations that have a high likelihood of being pathological. For each object and for a given passband, each measurement (by epoch) was subject to the following “interrogation”:

1. Is the object’s centroid located within 50 pixels of the edge of the respective CCD?
2. Are there any detected sources (including cosmic-ray hits) within 1 FWHM (of the PSF) distance from the object’s centroid?
3. Does the value of the fitted background, s , fall outside the range $s_2 \leq s \leq 2.s_{90} - s_2$, where s_2 and s_{90} are the 2nd and 90th percentile values, respectively, for the fitted value of the background for *all* stars on that image?
4. Does the reported measurement error exceed err_{lim} , as defined in Section 3?
5. Did DoPHOT assign the object a type other than 1 or 3 (which are for objects with an unambiguously stellar PSF; see Section 3 for DoPHOT types)?

If the answer to any of these questions is positive, the measurement was excised from further consideration. At least 15 measurements for a given object in a given passband must survive in order to proceed with variability assessment. Criterion 5 is particularly severe in eliminating faint measurements. For our primary purpose of detecting and measuring the RR Lyrae stars, this is not an obstacle (as will be demonstrated later), but it may well inhibit the detection of variables to the faint limits that the photometry would otherwise allow. However, it is clear that the “purity” of the variable candidate list declines rapidly if DoPHOT type 7 measurements (those for which the S/N is too low to unambiguously ascertain if they have stellar PSFs) are allowed.

In the final analysis, only 450,344 objects in u ; 1,082,121 in g ; 1,950,425 in r ; 2,509,906 in i ; and 2,347,075 in z passed the above “interrogation” and were examined for variability. These numbers correspond to about 20% of all objects detected on the best and deepest available images in the respective passbands. The process can be easily rerun with changes in any and all of the parameters mentioned here.

The variability search was carried out using the method laid out in Saha & Hoessel (1990). A reduced chi-square, χ_ν^2 , with respect to the mean value of available magnitude measurements is computed using the available magnitude measurements and associated reported errors. We used a bootstrap sampling of the magnitude and error measurements for each of the available epochs to generate a robust estimate for the χ_ν^2 , using 100 resamples. Ideally the χ_ν^2 for a non-variable (given the reported

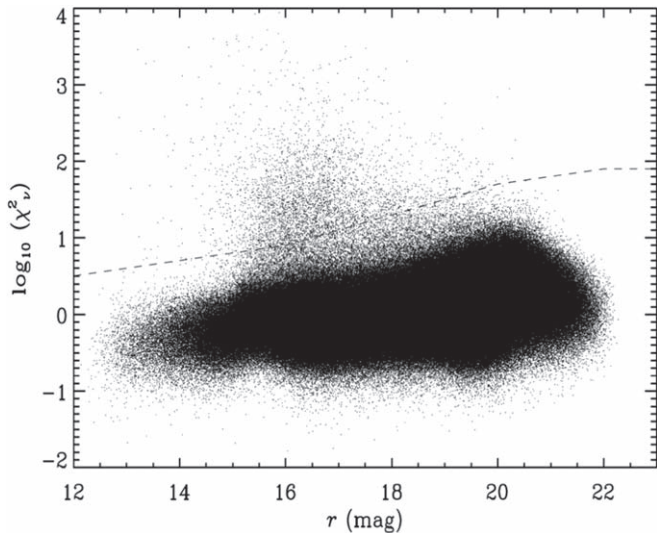


Figure 2. Individual values on a log scale of the reduced chi-square χ_ν^2 (as described in Section 4) as a function of the average brightness (r -band magnitude) for approximately 2 million stars in the r band. For accurate reported errors, and for a Gaussian error distribution for an unvarying object, the most probable value of χ_ν^2 is unity. Accordingly, the figure suggests that for the brighter stars, the reported errors are overestimates, while for $r > 17$ the distribution peaks close to $\log \chi_\nu^2 = 0$, indicating that error estimates reported by DoPHOT are reasonably correct. Objects with significantly higher values of χ_ν^2 are candidate variables. The program allows the user to interactively set the threshold for flagging something as a putative variable, such as by the dashed line shown in the figure. As described in the text, the χ_ν^2 values are computed for each object using a bootstrap procedure with 100 draws, which provides a more robust estimate by suppressing the contribution from one or two pathological extreme measurements of brightness.

noise) should hover around unity. However, since in reality the distribution of noise is not fully expressed by a single Gaussian, and because reported errors are themselves subject to bias, we see that the mean of χ_ν^2 can change weakly with the brightness (see Figure 2). Accordingly, the mode value of $\log \chi_\nu^2$ was calculated for 0.5 mag wide bins of mean magnitude, and an object was flagged as a variable if its $\log \chi_\nu^2$ is higher than the relevant mode value by 1.3 (i.e., 20 times or more higher than the mode). The program also allows the user to interactively set the detection threshold with varying brightness. The variable lists from the above analysis in each passband were merged. A total of 4877 putative variables were flagged with this procedure, where each candidate is flagged in at least one of the five passbands.

4.2. Identification of ab -type RR Lyraes and Derivation of Colors at Minimum Light

All of the 4877 candidate variables flagged previously were run through the period finding procedure described in Saha & Vivas (2017; hereafter PSEARCH) in “batch” mode using $\Delta\phi_{\max} = 0.05$ (as defined in their Equation (9)). We identified the highest resultant peak of the Ψ periodogram of PSEARCH for each object and the resulting folded light curves in all available bands were plotted. A visual examination of the plots very quickly reveals the objects that are possibly RRab (radially pulsating in the fundamental mode) variables. The PSEARCH code was rerun interactively with $\Delta\phi_{\max} = 0.02$ (for details see Saha & Vivas 2017) for the objects that were

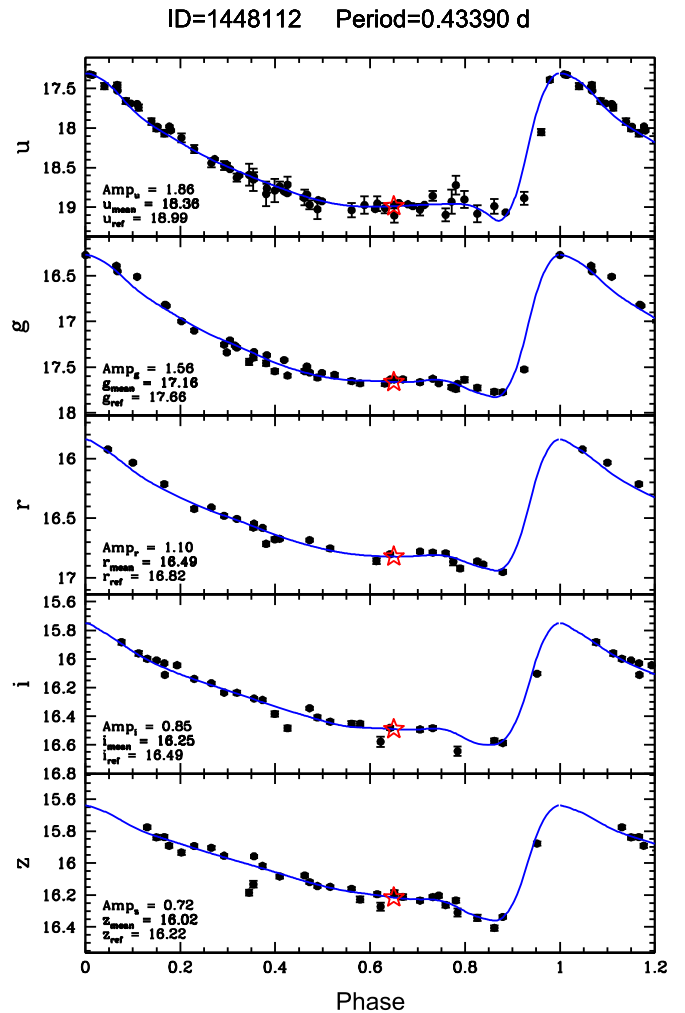


Figure 3. Example of light-curve and best fitted templates in $ugriz$ for one of the RR Lyrae stars in field B1. The red star indicates the magnitude at minimum light (m_{ref}), which was set to be measured at $\phi = 0.65$.

(The complete figure set [474 images] is available.)

flagged as possibly RRabs to confirm the classification and to select the most likely period from among any aliases.

The preliminary light curves mentioned previously for all the of the 4877 candidate objects reveal a wealth of different variables. Binaries with short periods that are relatively well sampled with the observed cadence show very convincing light curves, as do short period pulsators like δ -Scuti and/or SX Phe stars. Many RRcs can be discerned by their slightly skewed near-sinusoidal light curves, while those without perceptible skewness are likely hiding as indistinguishable from among contact binaries with sinusoidal light-curve shapes. There are also variables for which no believable folded light curves could be obtained. Their periodograms show peaks at much longer periods for which the data at hand cannot be used to derive believable periods. These are likely to be long period or semi-regular or irregular variables. Since the OGLE project surveyed the same region of the sky, and with much more extensive timing coverage than the present one (which was optimized to get light curves of the RR Lyraes), many of our identified variables can be matched to OGLE identified variables, for

Table 3
Photometry of ab-type RR Lyrae Stars in Field B1

ID	HJD—2,400,000.0	Filter	Mag	Error
1448112	56423.665618	<i>u</i>	17.528	0.012
1448112	56423.814222	<i>u</i>	18.799	0.015
1448112	56424.718744	<i>u</i>	18.923	0.014
1448112	56424.810501	<i>u</i>	18.971	0.015
1448112	56424.888096	<i>u</i>	19.067	0.016

(This table is available in its entirety in machine-readable form.)

which their variable classification is available. While their data are primarily in one band, the panchromatic information from the data set of our study here can be used in novel ways to develop new classification methods and is the subject of an ongoing study.

We then ran the list of 491 possible RRab stars through a template fitting program, from which the properties of the light curves (mean magnitude, amplitude, initial phase) were derived. This process is particularly important to define the initial phase (phase at maximum light) of the light curves. The use of templates is helpful when the observations do not sample well that part of the pulsation period. We used the library of light-curve templates set up by Sesar et al. (2010) from RR Lyrae stars in SDSS Stripe 82. The library contains between 10 and 20 templates in each filter for type-ab RR Lyrae stars, and only 1 or 2 for the types c. During the fitting process we allowed for variations around the period found by PSEARCH (± 0.001 day, in steps of 1×10^{-6} days), the observed amplitude (± 0.2 mag in steps of 0.01 mag), the magnitude at maximum light (± 0.2 mag in steps of 0.01 mag), and the initial phase (± 0.2 in steps of 0.01), which was initially set by the time of the observation with the brightest magnitude in the light curve. The best template is found from χ^2 minimization. Initially the fit is done only in the filter with the largest number of epochs available, which sets up the period and initial phase for that star. Then, the template fitting procedure is repeated for the other four filters but allowing variations only in the amplitude and maximum magnitude. Light curves and the fitted templates for all stars are available as Figure 3. They are also available via a Github repository.¹⁶ The epoch-by-epoch photometry in all bands for the bona-fide RRab stars is presented in Table 3.

During this process, we found 16 objects in the list to be poor fits to RRab templates. These objects were classified as other kinds of variables in the OGLE catalogs. In the final analysis, we have 474 surviving ab-type RR Lyraes, for which the periods, mean magnitudes, magnitudes at minimum light, and amplitudes in the 5 passbands are listed in Table 4. The mean magnitudes were calculated by integrating the template light curve in each band after it had been converted to intensity units. The magnitudes at minimum light correspond to the magnitude of the fitted template at phase $\phi = 0.65$. The same procedure was applied to the RR Lyrae stars in the globular cluster M5 presented by Vivas et al. (2017), whose calibration will be used here to estimate the reddening.

Table 4
Description of Table of RRab Stars and Their Fitted Parameters

Column	Description
1	Object Identifier
2	R.A. (J2000)
3	Decl. (J2000)
4	Fitted Period (days)
5	HJD—400,000. Reference Epoch of zero phase ($\phi = 0$)
6	No. of available <i>u</i> measurements
7	<i>u</i> -band amplitude
8	u_{mean} (mags)
9	u_{ref} (mags) [Fitted value at $\phi = 0.65$]
10	No. of available <i>g</i> measurements
11	<i>g</i> -band amplitude
12	g_{mean} (mags)
13	g_{ref} (mags) [Fitted value at $\phi = 0.65$]
14	No. of available <i>r</i> measurements
15	<i>r</i> -band amplitude
16	r_{mean} (mags)
17	r_{ref} (mags) [Fitted value at $\phi = 0.65$]
18	No. of available <i>i</i> measurements
19	<i>i</i> -band amplitude
20	i_{mean} (mags)
21	i_{ref} (mags) [Fitted value at $\phi = 0.65$]
22	No. of available <i>z</i> measurements
23	<i>z</i> -band amplitude
24	z_{mean} (mags)
25	z_{ref} (mags) [Fitted value at $\phi = 0.65$]
26	Cross-matched OGLE Identifier

(This table is available in its entirety in machine-readable form.)

4.3. Completeness Estimates

The correlation of our final list of RRab stars with the RRabs from the RR Lyrae stars compilation of Soszyński et al. (2014) from the OGLE survey (hereafter OGLE RRabs) allows us to make a quantitative estimate of the discovery completeness from *both* surveys.

The DECam pointings at the various epochs were intended to repeat exactly. Hence the excluded regions, such as from gaps between chips were also repeated, and any variables that occupy that excluded region would not be detected. Recall also that a measurement of any object that at a given epoch fell within 50 pixels ($\sim 13''$) of any chip's edge was discarded. With such caveats in mind, we denote the total number of RRab stars present on the complex operational portion of the DECam footprint by N . Let n_O , be the number of these actually present in the Soszyński et al. (2014) compilation and n_U the number found by us in this work. Let p_O and p_U denote the discovery completeness of OGLE RRabs and the present work, respectively. We estimate from counting the OGLE RRabs within the discoverable area of our B1 field that

$$n_O = N p_O \approx 560 (\pm 15), \quad (5)$$

where the uncertainty arises from the difficulty of counting stars in the avoidance zones within our footprint.

From our own data and procedures described previously, we have independently identified 474 ab-type RR Lyraes, so that

$$n_U = N p_U = 474. \quad (6)$$

Matching the list of RRabs from Soszyński et al. (2014) with ours using a 2 arcsec matching tolerance, we find that there are

¹⁶ <https://github.com/akvivas/Baade-s-Window>

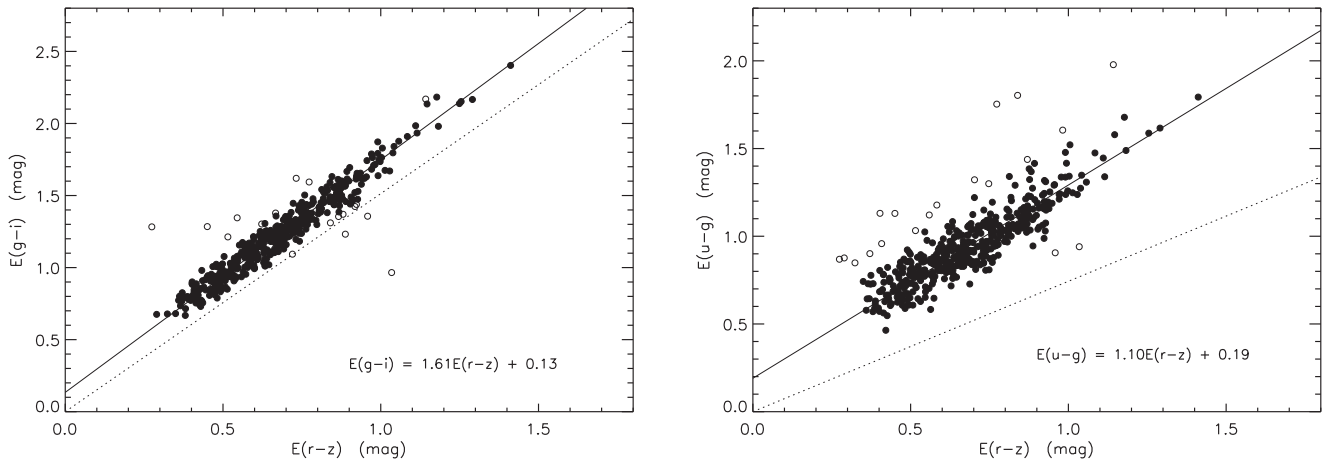


Figure 4. Color excesses in $E(g - i)$ vs. that in $E(r - z)$ as derived from the minimum light colors of individual RRAb stars for which the brightness at $\phi = 0.65$ could be determined in *all* five bands (left panel). Due to the large differential extinction in the field, the RRAb ensemble samples a large range of reddening. A straight line fit to the data, allowing errors in both axes and 3.0σ iterative rejection (rejected points shown as open circles), is shown, whose slope $E(g - i)/E(r - z)$ is a reflection of the reddening law. The 0.13 mag intercept is unexpected and is discussed in the text. The dotted line shows what would be expected from the O’Donnell (1994) reddening law with $R_V = 3.1$. The right-hand panel shows the same for $E(u - g)$ vs. $E(r - z)$: the intercept is slightly larger, as is the discrepancy of the slope wrt the O’Donnell law.

472 RRabs in common, so that

$$N p_O p_U = 472. \quad (7)$$

It follows from the above that

$$p_O \approx 0.996 \quad (8)$$

$$p_U \approx 0.843. \quad (9)$$

It should be emphasized that these numbers are valid for RRAb stars only. Other types of variables suffer different selection effects. Specifically our images typically have better seeing and greater depth than OGLE, but we have much fewer epochs and a shorter total time baseline. Consequently, we optimized our observing cadence for detecting RR Lyrae stars (our primary goal) at the expense of other kinds of variables with different temporal characteristics. OGLE has many more epochs and better coverage of the window function compared to the present study, albeit only in the i band.

5. Reddening from the RR Lyrae Colors at Minimum Light

Sturch (1966) showed that the $B - V$ colors of fundamental mode RR Lyrae stars (i.e., the Bailey ab-type) are invariant in the phase range $0.5 < \phi < 0.8$ (where the phase at maximum light is defined as 0.0) and that, aside from small metallicity and period dependent de-trending, the intrinsic ($B - V$) colors are the same from star to star to within a few percent. Thus these serve as standard color sources, and have been used to determine interstellar reddening, including calibrating reddening from HI maps and galaxy counts by Burstein & Heiles (1978). This paradigm has recently been re-examined using DECam filter passbands by Vivas et al. (2017), who have presented expected colors for several passband combinations (their Equation (1), Table 6, and Figure 3) from a study of the RR Lyraes in the globular cluster M5. Their minimum light colors are derived from fitted light-curve magnitudes at $\phi = 0.65$. Specifically, for zero reddening, we have from their paper that

$$(r - z)_{\min}^0 = 0.095 - 0.322(\log P)^2 \quad (\text{rms} = 0.016) \quad (10)$$

$$(g - i)_{\min}^0 = 0.347 - 0.973(\log P)^2 \quad (\text{rms} = 0.026) \quad (11)$$

$$(u - g)_{\min}^0 = 0.665 - 0.669(\log P)^2 \quad (\text{rms} = 0.029), \quad (12)$$

where P is the period in days and the 0 superscript implies intrinsic colors. The information in Table 6 of Vivas et al. (2017) also enables us to derive the intrinsic minimum light colors in any color combination as a function of period. We do not list them all here explicitly.

The fitted magnitudes at phase 0.65 (the middle of the phase range where Sturch demonstrated that colors are constant) of the individual RR Lyraes in Table 4 are listed in the same table. From these we can construct the observed $(r - z)_{\min}$ and $(g - i)_{\min}$ values for the RRabs, in Table 4, and obtain the color excess $E(r - z)$ and $E(g - i)$ from Equations (10) and (11). The differential reddening across the field provides an opportunity to study the relationships of reddening across different color combinations. Figure 4 shows the individual reddening values $E(g - i)$ and $E(u - g)$ as a function of the reddening in $E(r - z)$ for all the RRabs in Table 4. Both panels show a linear trend. The u filter has a small known red leak. For RR Lyrae stars, which are relatively blue, this should not have a noticeable effect. Further, if the reddening to M5 and field B1 were the same, the effect of the red leak would affect both fields equally, and the effect would be nulled out. However, as B1 has substantially more reddening, it is prudent to ask if this is a potential problem. We note that given the large range of individual reddening among the RRabs in B1, the effect of a red leak in the u band would express itself in the $E(u - g)$ versus $E(r - z)$ relation as a departure from linearity. We do not see such an effect in Figure 4, demonstrating that any adverse contribution from a u band red leak is below the accuracy imposed by the scatter seen in the figure.

The best fit (allowing for errors in both axes and utilizing iterative 3.0σ outlier rejection) that relates the reddening in the two cases is given by

$$E(g - i) = (1.614 \pm 0.019)E(r - z) + (0.134 \pm 0.013) \quad (13)$$

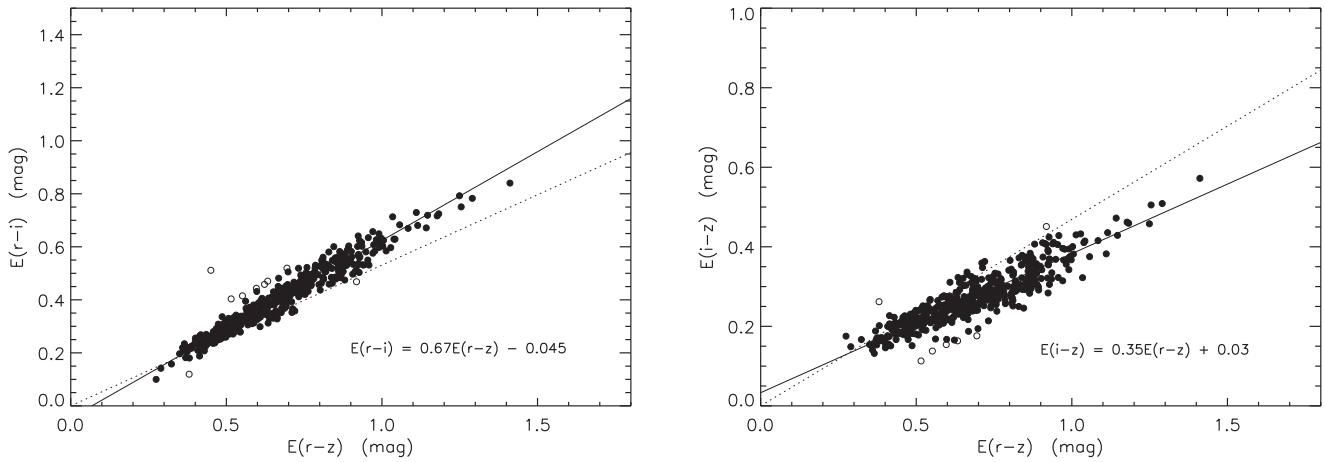


Figure 5. Same as Figure 4, but the left and right panels now have $E(r - i)$ and $E(r - z)$ as ordinate. Notice that unlike in Figure 4 the linear fits pass very close to the origin, well within expected errors. Note also that for $E(i - z)$, the fitted slope is shallower than for the (O’Donnell 1994) law, whereas the slopes for $E(g - i)/E(r - z)$, $E(u - g)/E(r - z)$ and $E(r - i)/E(r - z)$ are steeper than predicted by the O’Donnell law with $R_V = 3.1$.

and

$$E(u - g) = (1.101 \pm 0.026)E(r - z) + (0.191 \pm 0.018), \quad (14)$$

where the uncertainties are estimated from the scatter. The figure shows the fitted relations, as well as the expectation from an O’Donnell law (O’Donnell 1994) with $R_V = 3.1$. We see differences in fitted versus expected slope, but what is problematic is the vertical intercept, as we expect the relation to pass through the origin. We consider and discuss the following possible explanations:

1. Calibration errors/uncertainties in either the M5 reference data or the data presented here, or both. Since the data in both these figures come from observations taken on the same nights, this is unlikely. We have gone over the procedures several times to ascertain that a careless error has not been made.
2. Cumulative random errors in the photometric calibrations. Ascertaining zero-points for any one band for each of the M5 and current data sets can suffer from random errors of up to 0.02 mag, so each color can have zero-point errors of 0.03 mag. Each axis of these figures is a difference of the same color in B1 and M5, so the total uncertainty in the zero-point of each axis can be .04 mag. Given that the slope of $E(g - i)$ versus $E(r - z)$ is ≈ 1.6 , we can thus expect y -axis intercepts of ≈ 0.065 mag at the 1σ level due to systematic errors in measuring the $E(r - z)$ alone (due to a shift in the x -axis zero). If all errors add in quadrature, total rms uncertainty in the intercept is $(0.04^2 + 0.065^2)^{0.5} = 0.075$ mag. This makes the observed offset in $E(g - i)$ almost a 2σ effect. For $E(u - g)$, the offset is much larger, but metallicity differences between the globular cluster M5 and the RRabs in the B1 field can induce all or part of the observed discrepancy (see Figure 6 of Vivas et al. 2017) in $E(u - g)$.
3. The bulge RR Lyraes have different properties from those in M5. We are examining this possibility by studying several additional RR Lyrae bearing clusters

that differ from M5 in metallicity and Oosterhoff type. Our sample includes clusters in the bulge that have much higher metallicities and unusual period distributions relative to their metallicity.

4. There is some peculiar reddening that is shared equally by all objects (which means it must be relatively local before encountering a spiral arm where different lines of sight must produce differential extinction that cause the large spread in reddening) with a much steeper value of $E(g - i)/E(r - z)$. Since the RR Lyraes here are all piled up in the bulge, and we do not see any with $E(r - z) < 0.3$, there is some effect that is hidden from us. Some of our other fields, especially B5, which passes clear of the plane, may illuminate whether this is a possibility. The equivalent of Figure 4 for the other fields along different directions in the Galactic bulge may shed some light on whether this is plausible.

The behavior in color combinations with the r , i , and z bands do not exhibit an anomalous intercept. This is illustrated in Figure 5. The linear fits are shown below in Equations (15) and (16), and have intercepts entirely consistent with expected calibration uncertainties. However, the fitted slopes are steeper than predicted by O’Donnell (1994) with $R_V = 3.1$ for all cases except for $E(i - z)/E(r - z)$, signaling that the slope differences are not resolvable by a simple scaling of R_V , and shows a departure in shape from the O’Donnell law. This result is independent of the issue of the unexpected intercept:

$$E(r - i) = (0.669 \pm 0.009)E(r - z) - (0.045 \pm 0.006) \quad (15)$$

$$E(i - z) = (0.350 \pm 0.008)E(r - z) + (0.033 \pm 0.006). \quad (16)$$

Differences in slope are indicative of non-standard reddening, and we investigate the implications in what follows. The intercepts must be accounted for when investigating distances, but it takes some contortion (item 4 in the above enumeration of possible reasons) to argue that they arise from non-standard reddening. We keep this in mind in the arguments we make in the remainder of this section. Specifically, the analysis that

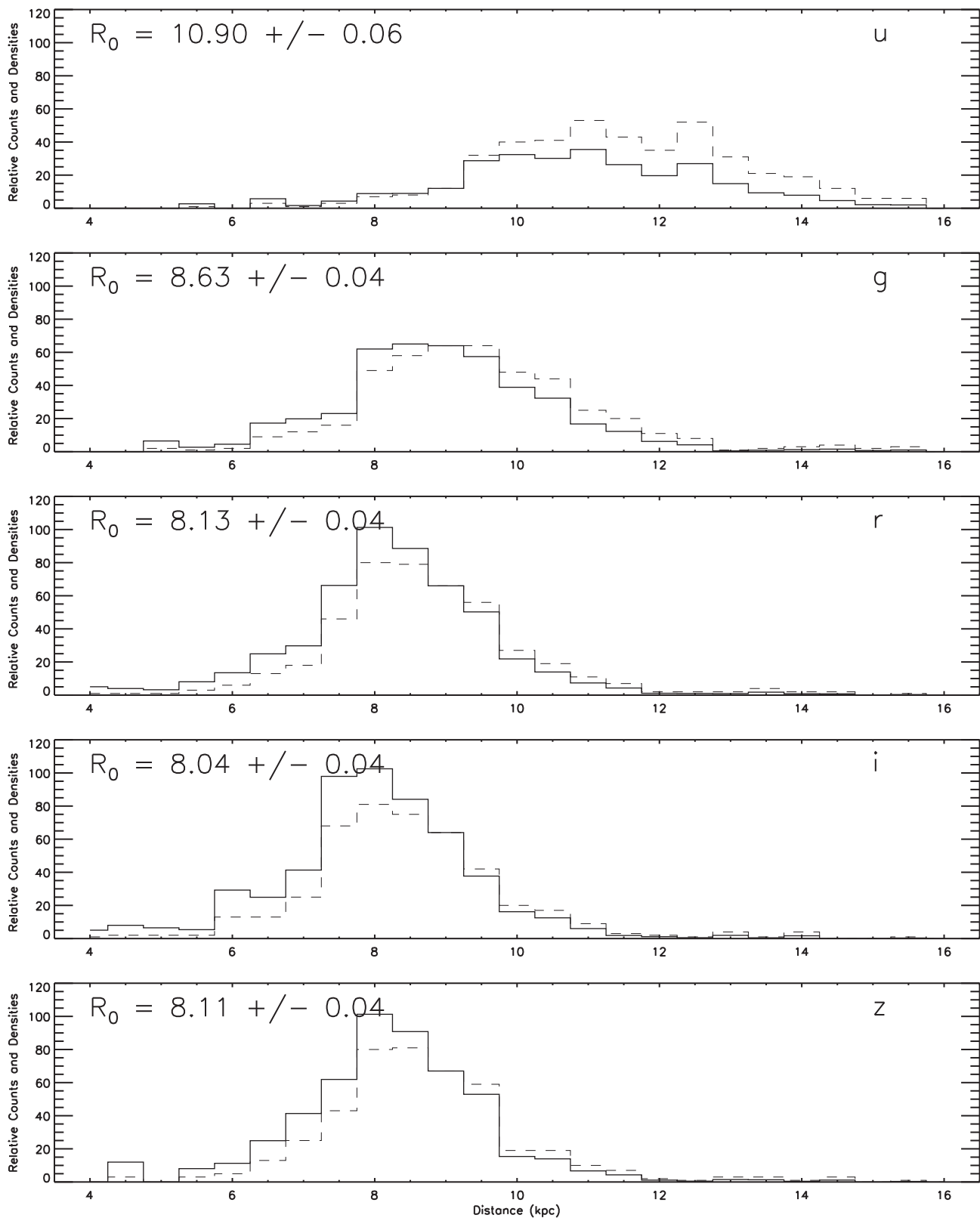


Figure 6. Distribution in distance of the RRab stars from Table 4 calculated from data in each of the five passbands, using the standard extinction law with $R_V = 3.1$, as enunciated in O’Donnell (1994). The dashed lines show the histogram of star counts, while the bold line shows relative density by correcting for the larger sampled spatial volume at larger distance by scaling each bin with star counts by $(9./d)^2$, where d is the distance for that bin. This scales the relative density to equal the star count at 9 kpc. Note the disagreement across the various passbands in distance to the peak of the distribution, as well as in the shape of the inferred distance distribution. Since in reality these cannot depend on the passband, it suggests strongly that the standard reddening law used to produce this figure does not apply for this line of sight.

follows does not depend upon the zero-point anomaly, but only on the slopes derived from the differential extinction.

We evaluate the effective wavelengths in each of the five passbands for an F5 spectrum and read the extinction at those wavelengths from the standard reddening law with $R_V = 3.1$ according to O'Donnell (1994). The F5 spectrum is a good approximation to an RRab star near minimum light, and thus appropriately matched for color excesses as measured from them. The extinction values in the five passbands determined in this way, and scaled so that $E(r - z) = 1$, provides the total to selective extinction ratios as follows:

$$\begin{aligned} A_u &= 3.92 E(r - z) \\ A_g &= 3.24 E(r - z) \\ A_r &= 2.26 E(r - z) \\ A_i &= 1.73 E(r - z) \\ A_z &= 1.26 E(r - z). \end{aligned} \quad (17)$$

We also quote from Equation (3) of Vivas et al. (2017), who calibrated the RRab absolute magnitudes in the globular cluster M5:

$$\begin{aligned} M_u(ab) &= (-0.10 \pm 0.24) \log P + (1.10 \pm 0.13) \\ M_g(ab) &= (-0.57 \pm 0.17) \log P + (0.43 \pm 0.12) \\ M_r(ab) &= (-1.28 \pm 0.11) \log P + (0.12 \pm 0.11) \\ M_i(ab) &= (-1.59 \pm 0.09) \log P + (0.07 \pm 0.11) \\ M_z(ab) &= (-1.68 \pm 0.08) \log P + (0.03 \pm 0.11). \end{aligned} \quad (18)$$

Given our observed mean magnitudes in each of these bands for each of the RRab stars in the B1 field, we derive individual distances to them. Figure 6 shows the histogram of star counts at the derived distances.

Since the line of sight passes very close to the Galactic center, the peak of the relative density histogram should occur very nearly at the distance of the Galactic center R_0 . There are well-defined peaks for the histograms in r , i , z near a distance modulus of 8.1 kpc, but shifts to 8.6 kpc in g , with the histogram peak less sharply defined. In u the histogram essentially disintegrates to a flat skewed extension, and the highest density is nearly at 10 kpc. We submit that this inconsistency between the various bands is due to the use of the incorrect reddening law, as already surmised from the disagreement between the observed reddening vectors versus those predicted by the standard reddening law. Differences in the reddening law affect not only the central tendency of the density histogram, but, because of the large differential extinction, also redistribute the relative distances among the RRab stars, changing the structure and shape of the density histogram from one band to another.

We can seek to derive the correct reddening law that will yield not only the observed reddening vectors, but also bring into accord the distance histograms in all five passbands. Since RR Lyrae, and especially the RRabs, are both standard candles and standard ‘‘crayons,’’ they lend themselves naturally to such an analysis. We show (in Section 8) that such an analysis yields a reddening law that can rectify disagreements of the distance distribution highlighted previously and makes them consistent across all five passbands.

5.1. Derivation of the Extinction from the Reddening

In light of the results and discussion provided, we must proceed with caution, clearly enunciating our assumptions so that the impact of this reddening ‘‘offset’’ (especially as seen in Figure 4) can be tracked and examined at any point. We will choose to use $E(r - z)$ as fiducial reddening, as the evidence from Equations (13) through (16) indicates that the r , i , z bands are better behaved, whatever be the source of difficulty with g and u . However, the discrepancy in slopes with respect to the standard reddening law, and the discordance of the space density histogram with distance along the line of sight, means that in order to calculate extinction from the reddening $E(r - z)$, we will be well served to derive $A_X/E(r - z)$ for any passband X for our line of sight from our own data. Since the distribution of the RR Lyraes along the line of sight is very sharply peaked at the Galactic center, we can exploit the standard candle property of RR Lyraes.

The absolute magnitude versus period relationships in Equation (18) are known to depend weakly on metallicity and are strictly valid for the metallicity of M5. However Walker & Terndrup (1991) showed from spectroscopic analysis the metallicity distribution of RR Lyrae in the bulge peaks at $[\text{Fe}/\text{H}] \approx -1.0$, whereas for M5 $[\text{Fe}/\text{H}] = -1.25 \pm .05$ from Dias et al. (2016). The similarity in metallicity supports using the absolute magnitudes from Equation (18). For the purpose of deriving extinction from reddening by the method described herein, any net offsets in the absolute magnitudes are not important, but their dependencies on period, as gleaned from Equation (18), are useful to consider.

The distance modulus μ_0 of any RRab star, its mean magnitude m_X , and its extinction A_X in band X are related by

$$A_X = m_X - M_X - \mu_0. \quad (19)$$

M_X is adopted for the appropriate band from Equation (18). $\mu_X = m_X - M_X$ is the apparent distance modulus in X . m_X , $E(r - z)$ for the RRabs are known from a combination of Table 4, Equation (18), and Section 5. Since M_X can have no explicit dependence on $E(r - z)$, we can write

$$\begin{aligned} \partial A_X / \partial (E(r - z)) &= \partial \mu_X / \partial (E(r - z)) \\ &\quad - \partial \mu_0 / \partial (E(r - z)). \end{aligned} \quad (20)$$

If all the RRabs are at the same distance (i.e., μ_0 is constant), then measuring $\partial \mu_X / \partial (E(r - z))$ would directly give us the value of $A_X/E(r - z)$. In the present case, μ_0 is not constant, but has a peaked distribution (we anticipate the result shown later in this paper that it peaks exponentially). If we can pick out the ones that are very near or within the sharp peak, and for which $\partial \mu_0 / \partial (E(r - z))$ is negligible (which is true if the bulge itself has insignificant reddening), Equation (20) would again yield the desired value of $A_X/E(r - z)$. Thus, given a large enough ensemble of RRabs, a wide enough range of $E(r - z)$, and a sufficiently peaked distribution in μ_0 , it should be possible to derive $\partial A_X / \partial E(r - z)$ from the slope $\partial \mu_X / \partial E(r - z)$. Note that if extinction/reddening within the bulge is *not* negligible, then objects at farther distance will on average have higher reddening, so that $\partial \mu_0 / \partial (E(r - z))$ is positive. This implies that the true value of $\partial A_X / \partial (E(r - z))$ is, if anything, *smaller* than the measured value of $\partial \mu_X / \partial (E(r - z))$, or that the above procedure yields at worst an upper bound on the total to selective extinction ratio. A potential further complication is that an individual RRab can have a metallicity different from the mean, producing some departure in absolute magnitude.

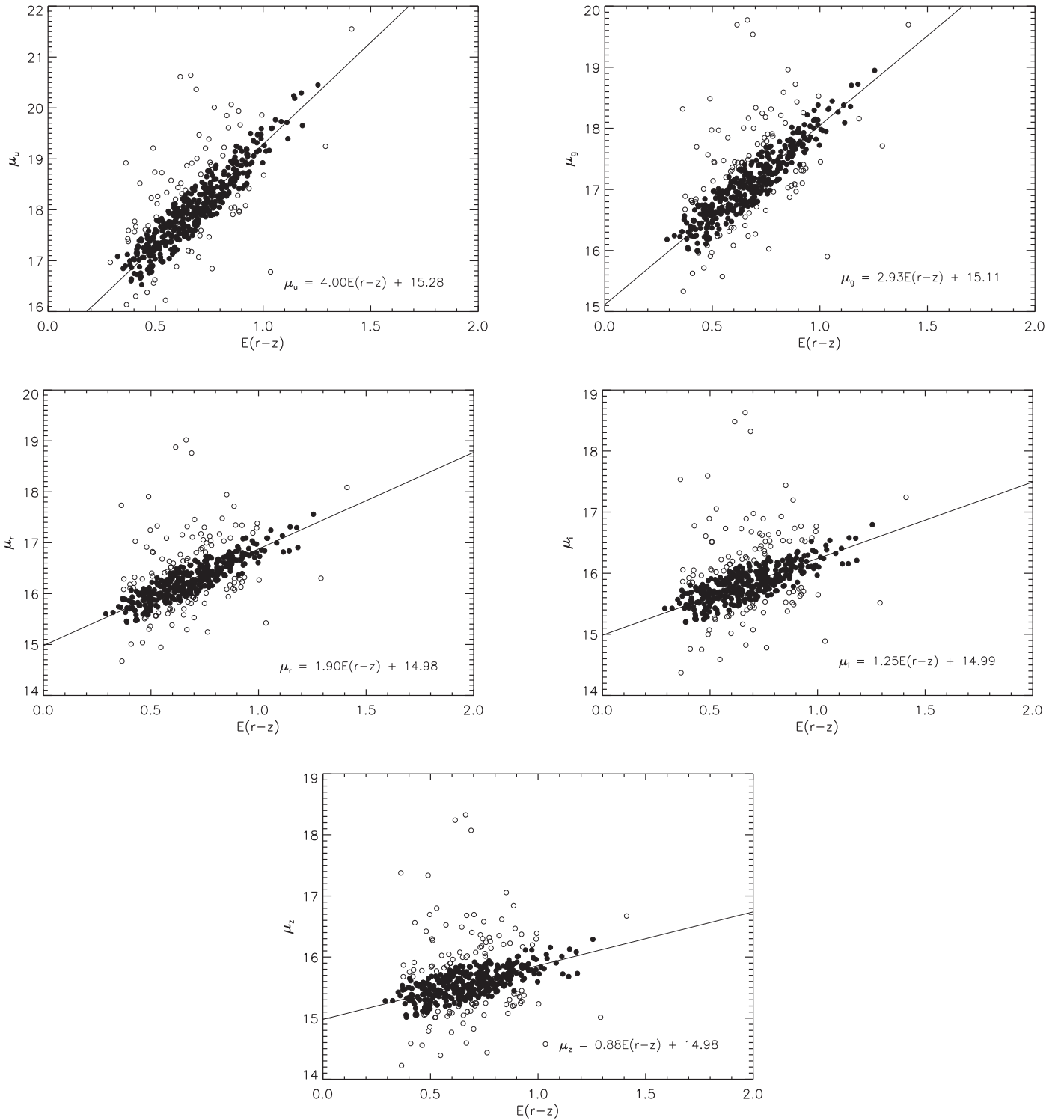


Figure 7. Apparent distance moduli in the five passbands of all individual RRabs in Table 4 for which there are available mean magnitudes in all five bands against their color excess $E(r-z)$. The linear fits, obtained by regression with errors in both axes and iterative 2σ outlier rejection, are shown in each case by the straight line. The stars used in the fit are indicated by filled circles. The fitted slope for each band is a determination of total to selective line-of-sight extinction for that band (see text).

However, this is not expected to exceed ~ 0.2 mag for any given such object, which is much smaller than the individual variations due to actual distance along the line of sight.

Figure 7 shows μ_X for all bands as a function of $E(r-z)$ for the ensemble of all RRabs for which mean magnitudes are

available from Table 4 for all 5 bands. Again, a linear fit with iterative outlier rejection was performed with uncertainties on both axes. A value of $\sigma = 0.05$ was used for $E(r-z)$ and $\sigma = 0.20$ was used for μ_X ; the substantially larger uncertainty for μ_X allows for the back to front rms depth in the distances of

individual RRabs about the distance at which the space density peaks. The iterative rejection threshold was set at 2σ . The intercepts in each case notionally provide the true mean distance modulus of the RRab in the sample. The few background and foreground RRabs are clearly seen as outliers in these figures.

The parameters and their uncertainties for the fitted linear regression for each of the five passbands are listed as follows:

$$\begin{aligned}\mu_u &= (4.003 \pm 0.087)E(r-z) + (15.281 \pm 0.061) \\ \mu_g &= (2.933 \pm 0.069)E(r-z) + (15.115 \pm 0.048) \\ \mu_r &= (1.898 \pm 0.058)E(r-z) + (14.978 \pm 0.041) \\ \mu_i &= (1.254 \pm 0.055)E(r-z) + (14.985 \pm 0.038) \\ \mu_z &= (0.880 \pm 0.053)E(r-z) + (14.981 \pm 0.037).\end{aligned}\quad (21)$$

As argued previously, the slopes in Equation (21) correspond to the values of $A_X/E(r-z)$. We should note that the slopes (as well as intercepts) in the provided derived relations are consistent within the errors with the corresponding slopes (and intercepts) in Equations (13) through (16). However, the larger uncertainties in Equation (21) are a result of the scatter introduced by the spread in actual distances to the individual RRabs. However, Equation (21) is necessary to infer the extinction. The color-to-color reddening relations (Equations (13) and (14)) alone do not allow us to do that. In the absence of independent determinations of the total to selective absorption, the default practice is to use a standard reddening law such as O'Donnell (1994), but Equation (21) makes it possible to check whether that is appropriate for the line of sight to our field B1.

It is worth pondering whether the presence of RR Lyraes in the two globular clusters, NGC 6522 and NGC 6528, which fall within our field B1, bias our results. NGC 6522, which was placed in the gap between two chips, has 11 RR Lyrae stars listed in the Clement catalog (Clement et al. 2001)¹⁷ within two half-light radii (r_h). All but two of these are masked by our pointing, and the ones that remain are first harmonic oscillators that are thus not in our list of RRabs. Similarly, NGC 6528 has only two known RR Lyrae associated with it, both within $2r_h$ (Skottfelt et al. 2015), one of which may be an RRab but is not in our list. Looking at it another way, there are three RRabs in our list within $5r_h$ of NGC 6522 (and none within $5r_h$ of NGC 6528). Even in the remote event that these three are bona-fide members of NGC 6522, removing them from the analysis does not change the derived coefficients in Equation (21) by more than a small fraction of the stated uncertainties.

The intercept values in Equation (21) strongly anti-correlate with the corresponding slope value. The numbers correspond to the effective true distance modulus of where along the line of sight the RR Lyraes pile up the most, but at farther distances the field of view samples a bigger volume, so this requires tempering before it indicates the distance at which the RRab density peaks. Also note that the value of $E(r-z)$ that follows from Equation (21) by subtracting A_z from A_r , while not identical to the input $E(r-z)$, is self-consistent within the errors. This is because we have fitted allowing uncertainties in both axes. Reading from Equation (21), we therefore adopt

$$A_i = 1.254 E(r-z) \quad (22)$$

$$A_r = 1.898 E(r-z) \quad (23)$$

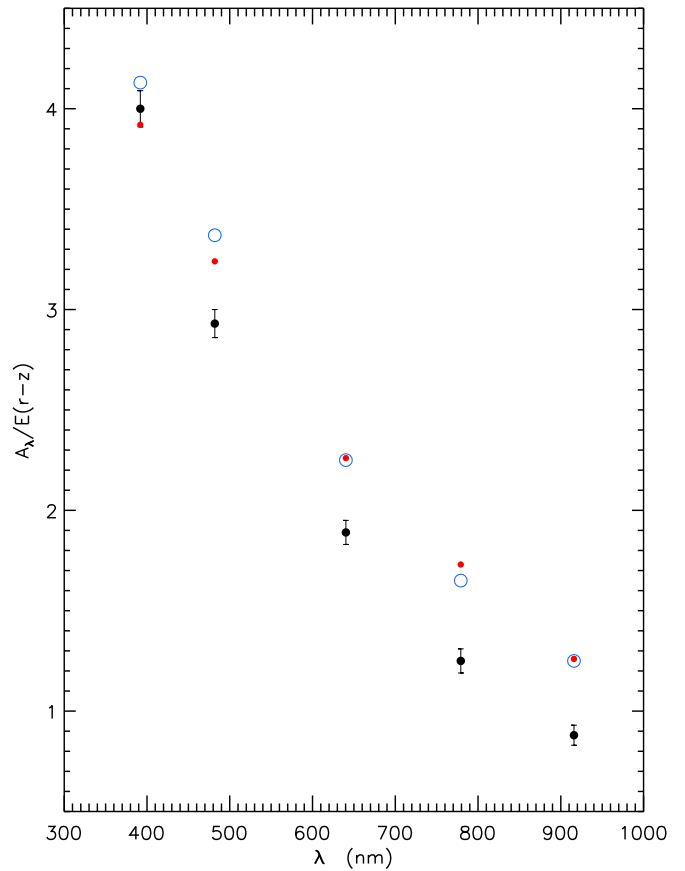


Figure 8. Comparison of the derived total to selective absorption for the five DECam passbands used here (by the black dots, along with their uncertainties) to the values implied by the $R_V = 3.1$ reddening law from O'Donnell (1994; shown by the red dots). The x -axis shows the effective wavelength corresponding to the passbands. The Fitzpatrick (1999) reddening law with $R_V = 3.1$, which is also commonly used in the literature as a default, is also shown for comparison (blue circles). Note that except in the u band, the differences between O'Donnell and Fitzpatrick laws with $R_V = 3.1$ differ by less than the difference of the law derived here with respect to either of them. As implied by the y -axis label, all three sets of points are normalized so that $E(r-z)$ is unity.

$$A_z = 0.880 E(r-z). \quad (24)$$

Recognizing that the accuracy of $E(u-g)$ and $E(g-i)$ from Equations (13) and (14) is far superior to the uncertainties presented in Equation (21), and that the determined value of A_i is both better constrained and less volatile with respect to errors in measuring $E(r-z)$ (because it has a multiplier of only 1.25 compared to 2.93 for A_g and 4.00 for A_u), it is prudent to determine A_u and A_g as follows (since they are better anchored to the data):

$$\begin{aligned}A_g &= E(g-i) + A_i = E(g-i) \\ &\quad + 1.254 E(r-z)\end{aligned}\quad (25)$$

$$\begin{aligned}A_u &= E(u-g) + A_g = E(u-g) \\ &\quad + E(g-i) + 1.254 E(r-z).\end{aligned}\quad (26)$$

For the RRabs themselves, the individual $E(g-i)$ and $E(u-g)$ are directly derivable using Equations (11) and (12). In what follows, we will only require Equations (22)–(26) to correct magnitudes for extinction, while we will correct (de-redden) colors using Equations (13)–(16).

For the five DECam passbands used, using the extinction law of O'Donnell (1994) with $R_V = 3.1$ gives $A_X/E(r-z)$ to

¹⁷ Updated version at <http://www.astro.utoronto.ca/cclement/cat>.

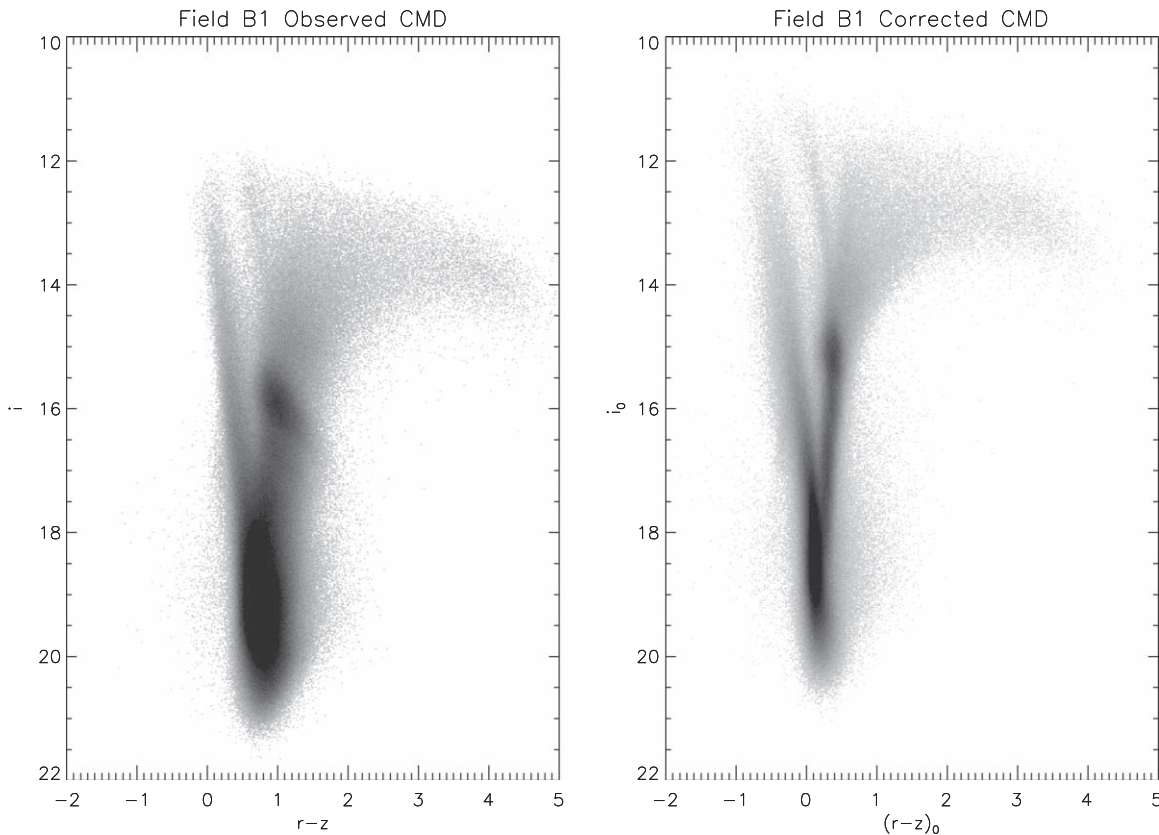


Figure 9. Observed CMD as i vs. $(r - z)$ (left panel). The right-hand panel shows the same CMD corrected for reddening and extinction using the procedure described in Sections 6.2 and 6.3. Note how in the left panel the red clump is extended along the reddening vector due to differential extinction, whereas in the reddening/extinction corrected right-hand panel the red clump falls in a very narrow color range, but shows vertical extension corresponding to the distance distribution. The various features are discussed in Section 6.4.

be 4.00, 3.26, 2.28, 1.73, and 1.27 for $X = u, g, r, i,$ and $z,$ respectively. Figure 8 shows both sets of values for $A_X/E(r - z)$. Since they are sufficiently different from our derived values, we adopt the latter as given in Equations (22)–(26).

6. Color–Magnitude Diagrams

6.1. Differential Extinction and Their Effect on the Observed CMDs

There are in all 9,623,873 distinct possible stellar objects in the master list of all objects in the field B1, as described in Section 3. All available measurements in all epochs in each passband were evaluated for the rejection criteria enumerated in Section 4, and if three or more such measurements in each band survived the cut, they were averaged. Because of the extreme crowding in the fields, there is a rather severe elimination of faint objects, which are measured cleanly only in the best seeing and deepest images. In all there are a little more than 2.5 million stars for which we have average magnitudes with this preselection in all of $g, r, i, z,$ and 906,449 where average mags in all five bands are available. The observed CMDs, with different colors in the abscissa but using i mags in the ordinate for all cases, involving various (but not exhaustive) combinations of the passbands are shown in the left panels of Figures 9–11. Differential reddening and extinction contribute to a washed out appearance: most notably the RC giants are smeared out along the reddening line for the redder abscissae, while for $u - g$ versus $i,$ where the clump’s extension into the blue is an intrinsic feature,

the reddening vector is no longer recognizable by the structure of the clump.

6.2. Correcting for Reddening and Extinction Using the RR Lyrae Stars

As the reddening and extinction to the individual RRabs are established as described in Section 5, we can apply these derived values to other stars close to them along the line of sight. However, we can see from the patchiness in the star counts on the images (especially in the u band) that the extinction varies on angular scales of an arcmin. The image of the full field was subdivided into rectangular bins, $30''$ on a side (the reason for the choice of bin size is explained below). If a bin contains one or more RRabs from Table 4, we assign the reddening and extinction from the RRab (averaging if there is more than one in a bin) to all the stars in that bin. For the first pass, stars in bins without an RRab are ignored. The resulting corrected CMD is shown in the left panel of Figure 12. Most notably, the clump stars no longer show the signature of differential extinction as they do in the uncorrected corresponding CMD in the left panel of Figure 10, showing that the method works as it should. However, there are only 31,804 stars in this CMD, compared to more than 2.5×10^6 stars that define the one in Figure 10, which is only 1.2% of all stars with adequate photometry. The corrected CMD is also over-represented by RR Lyrae stars because of how it was constructed (only bins containing an RRab were used). The clump of stars near $(g - i)_0 \approx 0.0$ and $i_0 \approx 15.5$ are thus the over-represented RRabs. Making the bins bigger increases

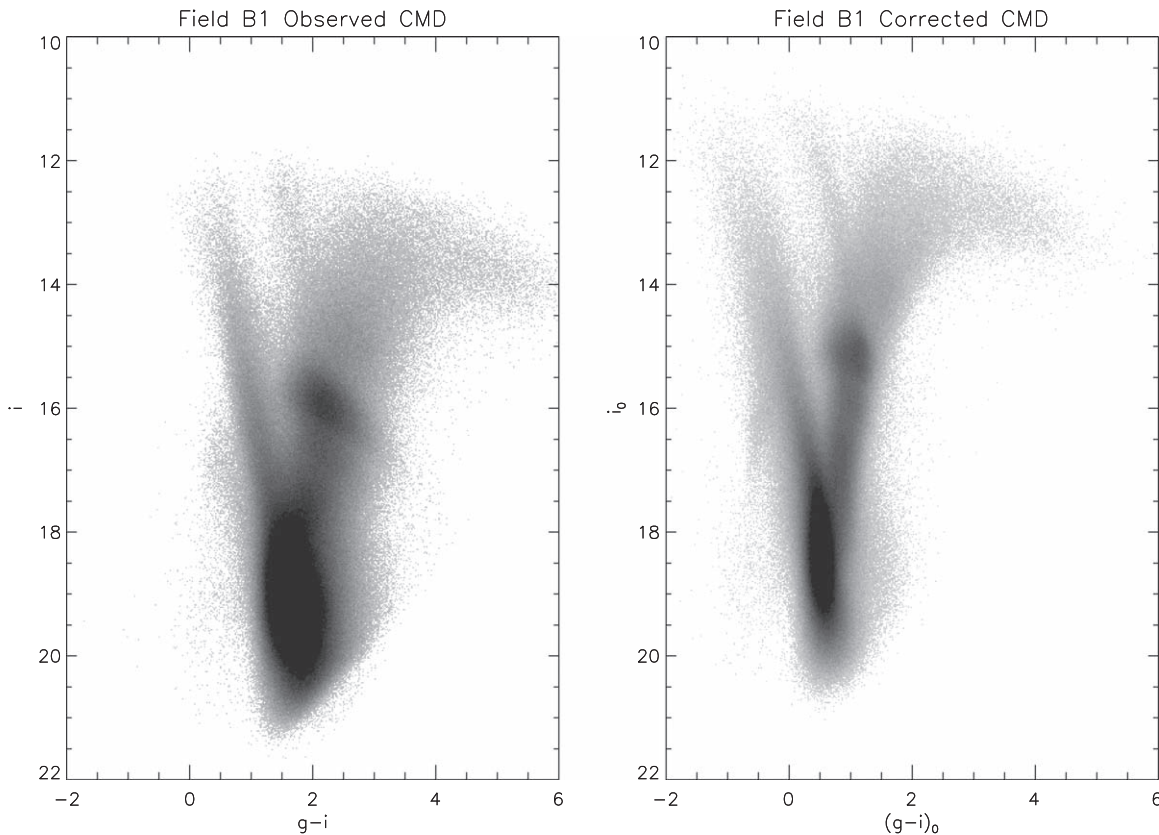


Figure 10. Same as Figure 9, but for i vs. $(g - i)$. See Section 6.4 for a discussion of the features.

the number of surrounding stars, but the angular structure of the differential reddening prevents us from using bins larger than than 60 arcsec, before deterioration from the differential effects becomes apparent. Clearly, there are too few RR Lyraes to directly de-redden all the stars in this way: we would need 50 times or more of them to do so.

We resort to a secondary method, anchored to the RRabs. The right panel of Figure 12 shows the de-reddened color-color diagram of the same stars that are in the left-hand panel. The primary shape of the distribution of stars in this color-color plane is an extension along a direction that is almost degenerate with the reddening vector (shown in the figure with a dashed line). However, the star counts at various points on the color-color diagram locus provide a third dimension, and there is a lot of structure in the relative counts of stars, so that it is in effect a de-reddened color-color histogram (CCH) of stars. We assert that, however complex the stellar population components may be along the line of sight, this CCH is self similar across the entire B1 field. Thus, the distribution shown in Figure 12 is the measured intrinsic CCH, made up of multiple sub-samples taken from over 460 locations randomly scattered across the DECam field of view. However, it is affected by the faint cutoff, which varies across the four passbands used, and because the faint cutoff for the de-reddened colors varies from place to place depending on the reddening and extinction. The former affects all field areas equally and thus should not adversely affect what we are about to do, but the latter could affect us if there are features in the CMD near the faint cutoff. Since the faint cutoff is on the the main sequence of bulge stars, and below the turnoff, variation in the cutoff of intrinsic magnitudes affects the CCH by changing the histogram value

at the cutoff colors. We show later, from a diagnostic from the de-reddening procedure described herein, that this is fortunately not a problem in the present case.

6.3. Correcting for Reddening and Extinction Using CCHs

We constructed a CCH using the stars shown in Figure 12 in the $r - z$ and $g - i$ color-color plane, with bin sizes of 0.02 mag along both axes. This represents the de-reddened CCH that we have asserted applies to all sub-regions within the ~ 3 square-degree DECam field. We denote this as the reference CCH. Consider the CCH constructed in the same way, but with uncorrected magnitudes and colors from any line-of-sight bin in the field. This should differ from the reference only to the extent of a translation in colors corresponding to the reddening of that field in $E(r - z)$ and $E(g - i)$. These shifts can be evaluated by a cross-correlation in the two color axes—that is, by determining the values of $E(r - z)$ and $E(g - i)$ that provide the best match to the reference CCH. It is possible to force a one-axis cross-correlation by demanding that the reddening obeys Equation (13), but allowing both color excesses to be derived simultaneously provides an important cross-check.

The result of this exercise is illustrated in Figure 13. Each point represents the derived value of $E(r - z)$ and $E(g - i)$ for one of nearly 40,000 line-of-sight bins. As mentioned previously, no external constraint was placed on the interdependence of the two axes. It is therefore very satisfying to see that the outcome is in accordance with Equation (13), which is represented by the dashed line. This is of course expected, because it is an essential ingredient of the reference CCH. If it were not recovered, it would signal that the

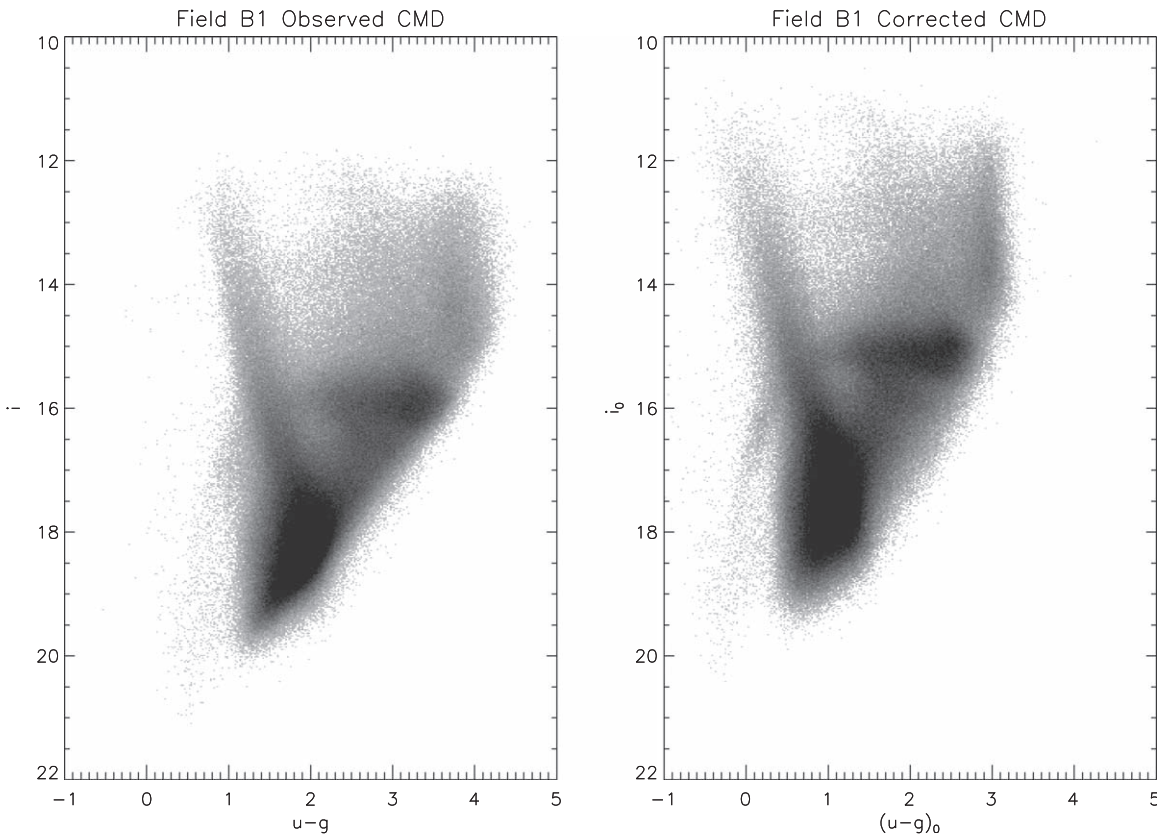


Figure 11. Same as Figure 9, but for i vs. $(u - g)$. The faint cutoff in the u band, which is much brighter than for the redder bands, explains the sharp oblique truncation on the lower right side of the CMD. Note how the clump stars spread to the blue due to intrinsic properties manifest in these passbands. See Section 6.4 for further discussion.

procedure for matching the observed CCH of each line-of-sight bin to the reference CCH is not working correctly. Rather, the fact that the slope and spread closely follow that of the left panel of Figure 4 assures us that the caveat raised at the end of Section 6.2 is not a manifest problem. It is also a diagnostic for ascertaining the optimal line-of-sight binning size. With the $30''$ bins, there are about 70 stars per bin that make up the observed CCH. There are places where there are fewer (e.g., when a bin straddles an inter-chip gap). To take such situations in stride, a condition was imposed to not use any bins where there are fewer than 10 stars with available averaged photometry in all of the u , g , r , i , z bands (instead for such bins we interpolate the results from neighboring bins). Smaller bins with fewer stars suffer from Poisson noise issues, and the equivalent of Figure 13 steadily deteriorates for bins smaller than $30''$ on a side, showing greater scatter. Bins that are much larger allow more variation in the reddening within their extent: with resulting ambiguity in the cross-correlation. To see this, we need to examine the two-dimensional structure of the correlation function peak, which we have found is often distended (or double peaked) along the reddening vector for bin sizes larger than $60''$ on the side. Our choice of $30''$ is guided by the desire to maximize the spatial resolution while minimizing the effects of Poisson noise from too few stars in a bin. This choice is customized for the B1 field. For other fields with different star densities and differential reddening structure, the optimal bin size is expected to be different. Figure 14 shows contours of the peaks in the cross-correlation matrix for nine randomly selected $30''$ bins. The peaks are highly elongated along the common direction of the reddening vector and the

shape of the color-color locus, but the contour levels point to a common center. The nine examples sample a range of reddening, as well as number of available stars in the respective CCH.

The individual $E(r - z)$ and $E(g - i)$ values thus determined for each 30 arcsec square line of sight can then be used to calculate the reddening in other colors using Equations (14) through (16). The extinction values in all five bands can be computed using the coefficients on $E(r - z)$ in the array of Equation (21), but ignoring the offsets therein. For each bin, de-reddened colors and extinction corrected magnitudes in all five bands for all stars in that bin can be obtained in this way, and the accumulated results for the entire field can be derived. The resulting CMDs are shown in the right-hand panels of Figures 9–11.

6.4. Salient Features in the Corrected CMDs

The efficacy of our procedure is immediately clear upon comparing the left and right panels of Figures 9–11. The difference is most striking for the $(r - z)$ versus i CMD, where in the corrected version the RC stars are gathered into a narrow color range, but with a vertical extent exceeding 0.5 mag from a combination of distance spread and possibly from stars of different ages. Both the lower main sequence and the sub-giant branch are much narrower in the de-reddened CMD, as we would expect. The corrected CMD shows that the red giant branch (RGB) and any asymptotic giant branch (AGB) stars fan out over a considerable color range, indicating a wide range of metallicities, as is already known from spectroscopy of bulge giants (e.g., Schultheis et al. 2017). The bright plumes of

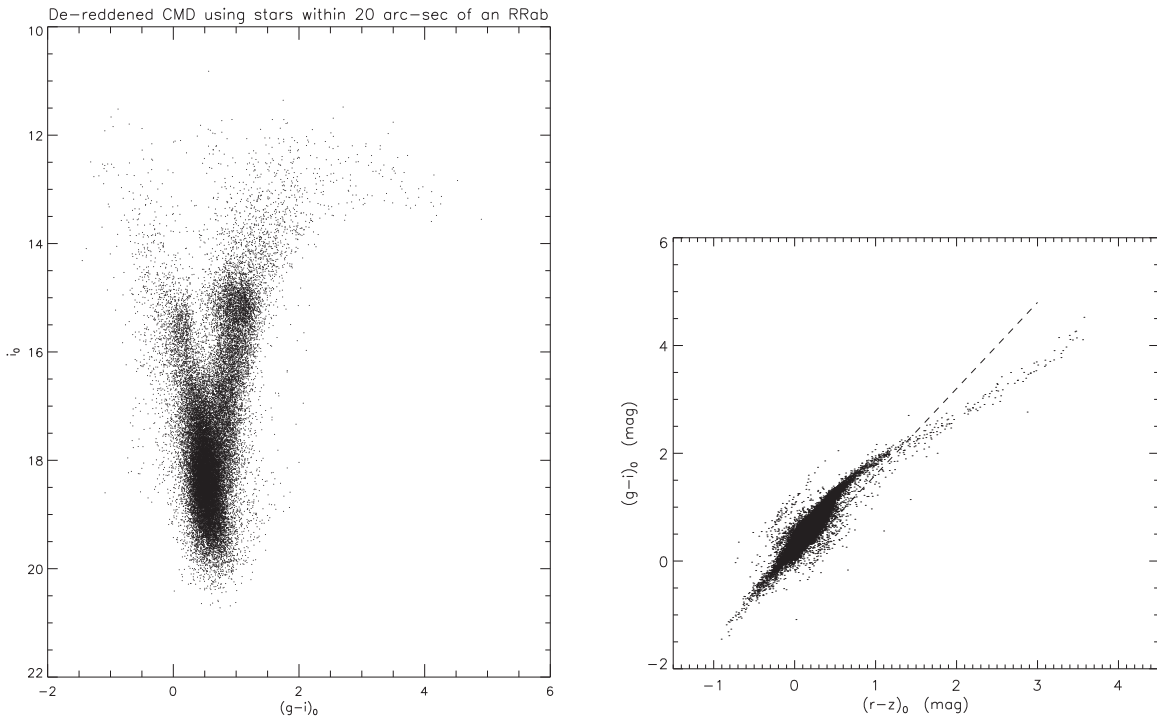


Figure 12. Extinction corrected CMD in i vs. $g - i$ for stars around RRabs in Table 4 (left panel), using the extinction correction derived from the RRab. Note how the clump stars have lost their extension and form into a well-defined blob. The right panel shows the reddening corrected color-color diagram using the same stars corrected for reddening and extinction in the same way. The dashed line is the reddening vector with the slope from Equation (13). See text for further details.

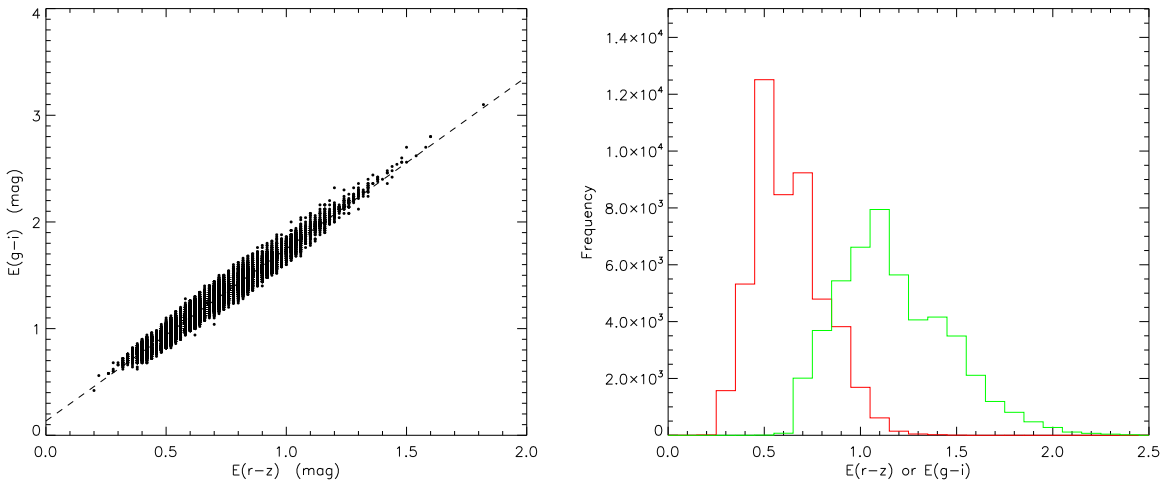


Figure 13. In the left panel, each point shows the derived $E(r - z)$ and $E(g - i)$ along a $30'' \times 30''$ sight line within the B1 field, computed using the procedure described in Section 6.3. The dashed line is not a fit to the points, but represents Equation (13), which is derived solely from the RRabs. In the right panel, the histograms of reddening values over the field area are shown: red for $E(r - z)$ and green for $E(g - i)$.

the bluest stars, however, appear to be *more* washed out in the corrected CMDs. This is because the reddening estimates are anchored by the RR Lyrae stars, which are clumped in the bulge, whereas the bright blue stars are foreground disk stars, for which the reddening has been overestimated: thus the “corrected” colors and magnitudes for these stars are incorrect.

There are two additional curious features in the corrected i versus $(r - z)$ CMD: a plume of stars extending from the top of the clump star locus, arcing to the blue with increasing brightness ($0 < (r - z)_0 < 0.5$ and $i_0 < 14.7$) and a sharpish blue edge for the RGB-like stars. These features occupy the expected location for evolved stars where helium ignition in the core occurs before the core becomes degenerate, and the star

ends up either as a red supergiant (that appears here as a pile up of RGB stars along a blue edge) or on the blue extremity of the helium burning “blue loop.” However, such locations in the CMD are populated by stars that are more massive than ~ 2.5 solar masses, implying that they are relatively young with ages of about 1 Gyr or even less. The “blue loop” track is clearly visible also in the i_0 versus $(g - i)_0$ CMD, but the putative red supergiants are indistinguishable from the rest of the RGB/AGB stars. Note that unlike the foreground main-sequence stars, the “blue loop” plume appears sharper and more tightly bound in color after it is de-reddened, signaling that they are located beyond the distances where most of the reddening takes place. The fact that the structure of the plume continues to stay

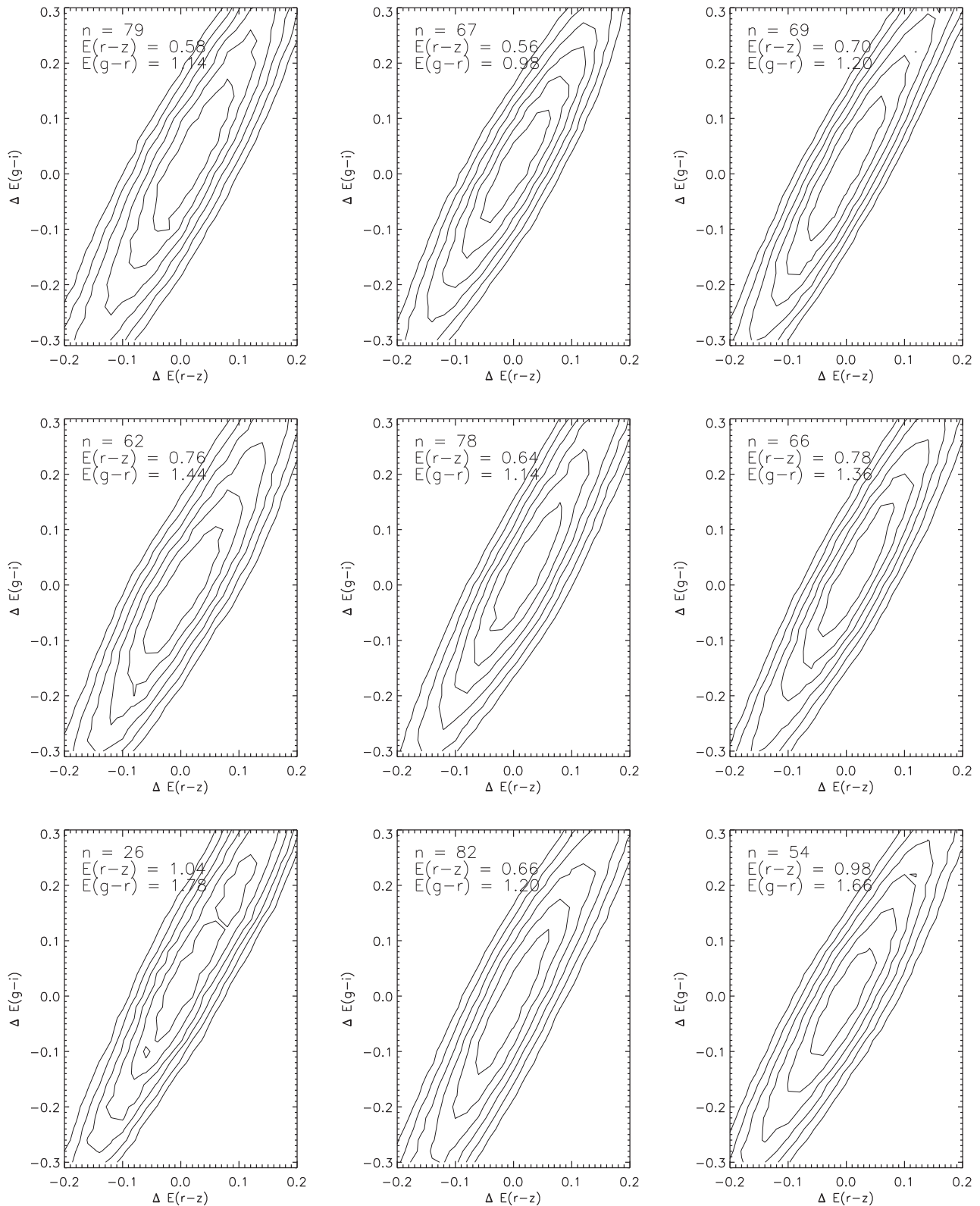


Figure 14. Contours of peaks in the cross-correlation matrix in the $E(r-z)$ - $E(g-i)$ plane for 9 (out of more than 37,000) randomly selected 30 arcsec square angular bins, used in the color-color histogram matching procedure described in Section 6.3. The contour innermost contour is at 90% peak value, proceeding outward at 10% intervals. Each example is annotated with the derived values of $E(r-z)$, $E(g-i)$, with the contours showing the correlation matrix centered about those values. The number of available stars, n , in the bin is also shown. Except when n is very small, the contour levels have a common center and are evenly shaped. The elongation in the contour ellipses is due to the degeneracy of the reddening vector with the shape of locus of stars in the color-color histogram. Uncertainties in centering on the peak appear to be consistent with the scatter seen in Figure 13.

Table 5
Mean Magnitudes of All Stars Used in the CMDs

R.A. (J2000) (degrees)	Decl. (J2000) (degrees)	u (mag)	$\sigma(u)$ (mag)	g (mag)	$\sigma(g)$ (mag)	r (mag)	$\sigma(r)$ (mag)	i (mag)	$\sigma(i)$ (mag)	z (mag)	$\sigma(z)$ (mag)	$E(r-z)$ (mag)
270.554370	-31.002110	20.134	0.008	18.977	0.007	18.451	0.005	18.186	0.005	0.88
270.562700	-31.001770	21.355	0.026	19.687	0.032	18.845	0.018	18.457	0.020	0.88
270.554960	-31.002100	20.623	0.012	19.445	0.008	18.810	0.007	18.481	0.008	0.88
270.561610	-31.002010	21.116	0.018	19.770	0.012	19.141	0.010	18.799	0.010	0.88
270.563130	-31.002290	21.582	0.025	20.244	0.013	19.733	0.017	19.428	0.011	0.88
270.558400	-31.004000	18.508	0.009	16.790	0.005	16.068	0.006	15.825	0.004	15.747	0.004	0.88
270.559340	-31.005540	21.608	0.032	18.413	0.006	16.751	0.007	16.004	0.004	15.585	0.004	0.88

(This table is available in its entirety in machine-readable form.)

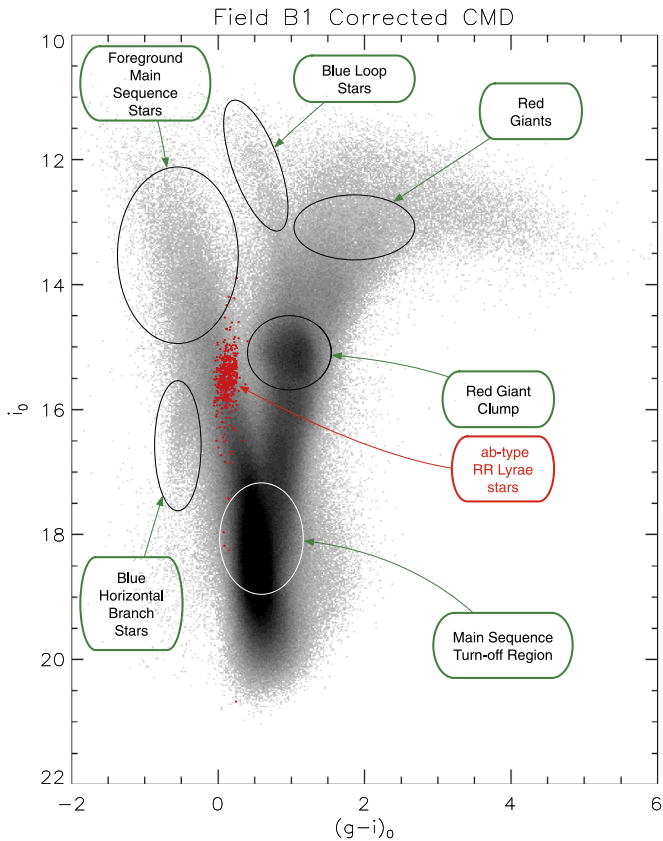


Figure 15. Same as the right panel of Figure 10, but with labels marking the salient features discussed in Section 6.4.

well bounded in color at all brightness levels, and that it arcs to the blue as it gets more luminous, are arguments that they are very unlikely to be foreground RC stars.

Figure 15 is a re-display of the right-hand panel of Figure 10, but with labels pointing out the features mentioned previously as they appear on the i_0 versus $E(g-i)_0$ CMD. There is a general broadening of features in this plane relative to the i_0 versus $(r-z)_0$ case, consistent with the fact that age and metallicity effects exhibit larger differences as we move to bluer colors. Nevertheless, the near vertical feature near $(g-i)_0 = -0.5$ and $i_0 > 15.8$ is more clearly expressed in the i_0 versus $(g-i)_0$ CMD, which is undoubtedly the extension of the horizontal branch as it “droops” in the blue. Note also that the RC stars are not as tightly confined in color in $(g-i)_0$ as they are in $(r-z)_0$, very likely because of the metallicity spread among the stars. Past attempts to de-redden using the RC stars

(e.g., Kiraga et al. 1997) using colors like $V-I$ would have suffered from the uncertainty and spread of intrinsic colors among the clump stars in the bulge.

The CMD in i_0 versus $(u-g)_0$ is severely cut off in the red because the u -band sensitivity of DECam as well as the more severe attenuation due to dust in u imposes a much brighter faint limit. The pileup of bright-red stars against a red limit near $(u-g)_0 \approx 3.0$ is likely the result of a red leak in the u filter. The highlight of this version of the CMD is that it stretches out the track of stars in their post-helium flash phase, emphasizes the color extension of the RC, prominently traces the entire extension of the horizontal branch, and sharply delineates the “droop” in the far blue range of the horizontal branch.

Figure 16 shows the observed (left panel) and corrected (right panel) CMD with u versus $u-g$, which is the bluest possible CMD rendition of our data where reddening and extinction express themselves maximally. The mean colors and magnitudes of the ab-type RR Lyrae stars are shown by the green points. On the uncorrected CMD, the RRab distribution is extended along the reddening vector, whereas in the corrected CMD they are distributed vertically in correspondence to their individual distances along the line of sight. Notice how the RRab distribution peaks where it intersects the horizontal branch (which in this color–magnitude configuration gets brighter in the blue relative to the clump). This particular representation of the CMD uses the color and magnitude most affected by reddening, so this consistency in the outcome of our de-reddening is gratifying.

Table 5 lists the positions, observed magnitudes, and derived values of $E(r-z)$ for all stars used to produce the CMDs.

6.5. A Spectroscopic Preview of the “Blue Loop” Stars

There are more than 1200 stars in the “blue loop” feature. If this is confirmed as such, then this is just the high-mass end of the IMF for stars with ages of order a few hundred Myrs. Ten of the objects falling within this blue loop from this sample of stars were also observed as part of the Apache Point Observatory Galactic Evolution Experiment (APOGEE), which is one of the experiments from SDSS III/IV (Abolfathi et al. 2018). APOGEE is a high-resolution spectroscopic ($R = 22,400$) survey in the near-IR ($\lambda = 1.51\text{--}1.70 \mu\text{m}$) that targets, primarily, red giants from all Galactic populations; it is planned to have observed $\sim 500,000$ stars by 2020 (Majewski et al. 2017; Jönsson et al. 2018; Holtzman et al. 2018). Survey results from APOGEE include stellar parameters (effective temperature, T_{eff} , surface gravity [as $\log g$], and microturbulent velocity), precise radial velocities, and detailed chemical

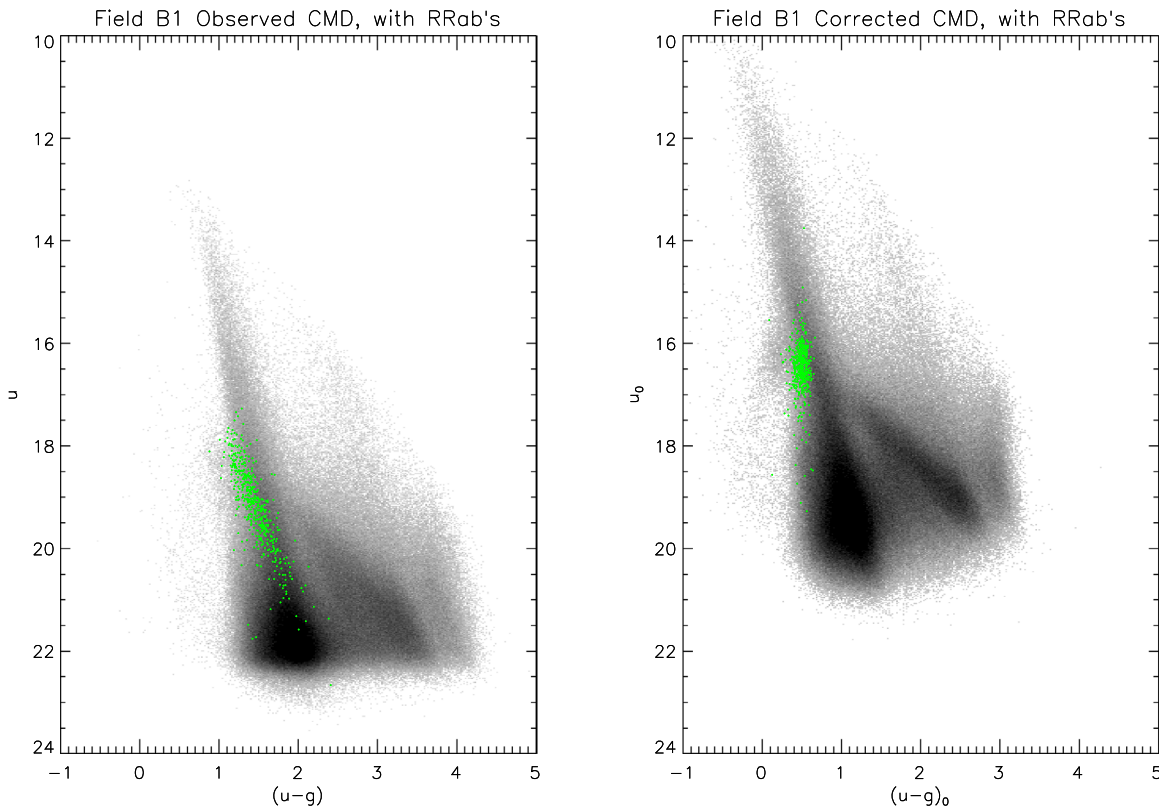


Figure 16. Left panel shows the observed CMD of field B1 with i vs. $(u - g)$. The green points mark the mean values for the ab-type RR Lyraes. Their locus is spread out along the reddening vector, plus some vertical spread from the spread in distances. The right panel shows the reddening and extinction corrected CMD in the same bands. Note how the RRab stars line up within a narrow vertical range, lending credence to the correction procedure employed.

abundance distributions from, typically, 15 elements. These results are derived from an automated analysis package called the APOGEE Stellar Parameter and Chemical Abundance Pipeline (ASPCAP; García Pérez et al. 2016).

The 10 red giants observed by APOGEE that are included in this study have ASPCAP calibrated parameters derived in the latest SDSS public Data Release 14 (DR14¹⁸). A separate paper (V. Smith et al. 2019, in preparation) will present a detailed analysis of these 10 stars, while DR14 ASPCAP results will be discussed here. The effective temperatures and surface gravities of these red giants are consistent with their being core-He burning giants, with a small range in T_{eff} and $\log g$: the mean values and their standard deviations are $T_{\text{eff}} = 4765 \pm 110$ K and $\log g = 2.6 \pm 0.2$. The metallicities of this sample of red giants are interesting, as all are quite metal-rich, with values of $[\text{Fe}/\text{H}]$ from $\sim +0.1$ to $+0.4$, which places them as likely members of the bulge, based on the observed distribution of metallicities of APOGEE bulge stars (e.g., García Pérez et al. 2018; Zasowski et al. 2019). The mean value for the 10 giants is $[\text{Fe}/\text{H}] = +0.25 \pm 0.10$.

Of interest to this study are values of the carbon-to-nitrogen ratios, C/N , in these core-He burning stars. Early stellar evolution models (e.g., Iben 1964) predicted that the C/N ratio in red giants, after the completion of the first dredge-up, will depend on the stellar mass. The relation between C/N and red giant mass is due to the deep convective envelope of a red giant, which mixes material to the stellar surface that has undergone H-burning via the CN-cycle, where ^{12}C has been partially processed into ^{14}N , leading to lower values of C/N relative to the main-sequence

values. More massive red giants have both deeper convective envelopes, as well as higher internal temperatures, so the increase in the surface ^{14}N and decrease in the surface ^{12}C abundances are larger, resulting in lower values of C/N with increasing red giant mass. Martig et al. (2016) have recently calibrated the relation between C/N and red giant mass, using a combination of APOGEE spectra and *Kepler* asteroseismology (Pinsonneault et al. 2014), resulting in mass estimates with rms errors of $\sim 0.2 M_{\odot}$. The change in C/N is largest between about $1\text{--}2 M_{\odot}$, making it useful for estimating ages over a range of about $1\text{--}10$ Gyr. The values of the C/N ratio in these 10 red giants display only a small scatter, with a mean value and standard deviation of $\langle [\text{C}/\text{N}] \rangle = -0.55 \pm 0.12$; based upon Martig et al. (2016), this indicates a mass of $\sim 1.5\text{--}1.7 M_{\odot}$ for this sample of bulge core-He burning giants. As these particular stars targeted by APOGEE are not the most luminous of the stars covered in the DECam sample, there are more luminous, and thus more massive, and even younger members of these clump giants.

7. The Reddening Map

The procedure described in Section 6.3 produces reddening values in $E(r - z)$ and $E(g - i)$ for each 30 arcsec square cell over the field of view of DECam, except where there are too few stars with reported mean magnitudes in g , r , i , z . These maps can be interpolated to bridge gaps (where there are too few stars). FITS images of these maps (with WCS encoding of R.A. and decl.) are available as data behind the figure, as well as in a Github repository.¹⁹ The map of $E(g - i)$ is shown in Figure 17.

¹⁸ <https://www.sdss.org/dr14/irspec/>

¹⁹ <https://github.com/akvivas/Baade-s-Window>

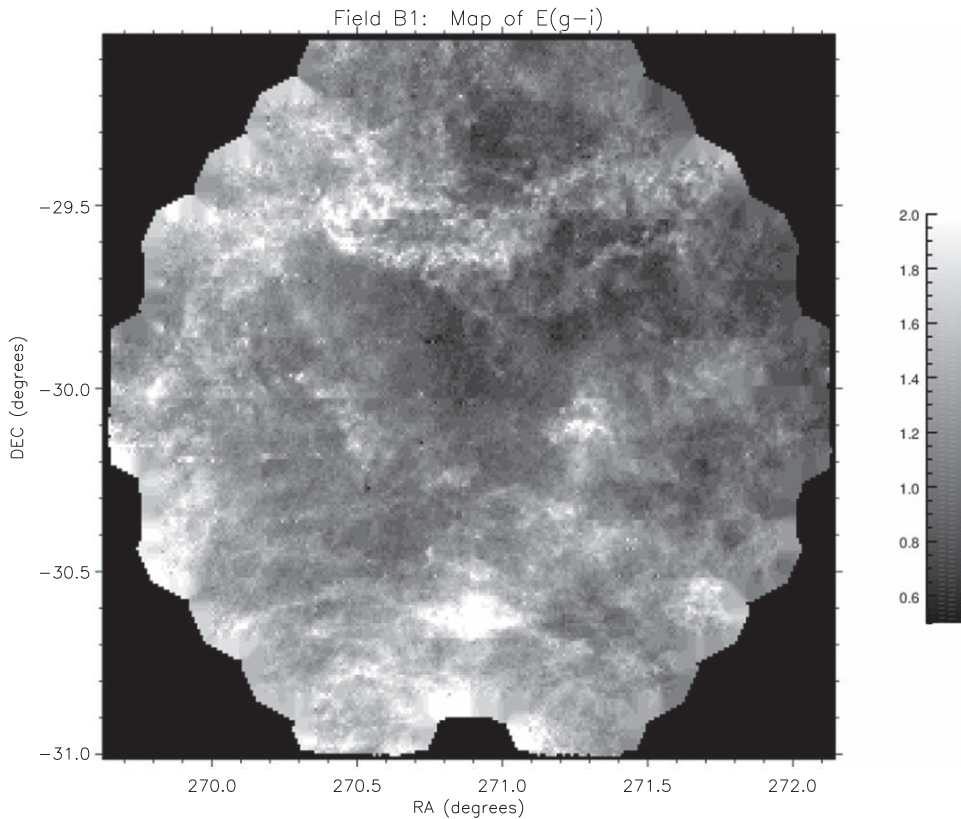


Figure 17. Map of reddening values in $E(g - i)$ to the Galactic Bulge derived in this paper from the color–color diagram correlation and the minimum light colors of RRab stars. Dark areas correspond to lower reddening and higher transparency, while lighter areas indicate higher reddening. This map is very similar to the dust map from Schlegel et al. (1998) of the same region, but has at least 10 times better linear resolution, and while it differs quantitatively, it is a good structural match to the 30 arcsec resolution A_V map of Stanek (1996) derived from Red Clump stars. The $E(g - i)$ and $E(r - z)$ maps are provided in FITS format as data behind the figure. The data used to create this figure are available.

The central part of the reddening map in Figure 17 shows relatively higher transparency without too much spatial variation in the reddening, and corresponds to the area chosen by Baade (1946) to peer close to the Galactic center. There is considerable patchiness outside this central window, with blobs and filamentary structures from arcminutes scales on up to the better part of a degree. Also visible are ring-shaped structures with relatively low contrast scattered over the entire field that appear to be shells of dust. They range in size from about 5 to 15 arcmin in diameter. These are likely to be ejecta from massive stars driven out by winds. Given the crowding in the field and irregularities in the shapes of the rings, we are unable to find any unambiguous visual correspondence of the ring centers with bright stars. We wonder whether having very short lives, such stars have long disappeared, but we are not in a position to know how long the bubbles would last before they dissipate.

8. Tracing the Bulge Geometry with the Fundamental Mode RR Lyraes

8.1. The Distance to the Galactic Center

Consider a heliocentric Cartesian coordinate system, where the z -axis points to the Galactic center, the x -axis is in the direction of the Galactic longitude l , and the y -axis points toward the north Galactic Pole (NGP). The projection on the z -axis of a point in space at a distance d from the Sun with

Galactic coordinates l and b is then

$$z = d \cos l \cos b. \quad (27)$$

The volume density in space of the RRabs of Table 4 in z is expected to peak at the distance R_0 to the Galactic center, provided the spatial distribution of the RRabs is spherical. However, for very small values of l and b , the effects from non-sphericity in the distribution are small. For the stars in field B1, with direction centered at $l < 2^\circ 05$ and $|b| < 5^\circ 0$, the product of the cosine terms in Equation (27) differ from unity by less than 0.5%, which mitigates any effects from moderate azimuthal and polar asymmetries in the density distribution. In fact, for B1, the peak in the distribution of d is by itself a measure of R_0 to within a percent if no azimuthal or polar asymmetries are present.

Since we have the individual reddenings (Equation (10) combined with observed minimum light colors from Table 4) and extinctions (using Equations (22)–(26)) as well as mean observed magnitudes m_X in any band X for the individual RRabs in Table 4, we can calculate their extinction corrected mean magnitudes m_X^0 . We get their absolute magnitudes M_X from Equation (18) using the period for the individual star from Table 4, which yields the distance modulus $DM_X = (M_X - m_X^0)$ for stars for each of the five passbands. The distance d_X to an individual star calculated from data in the X band is then given by

$$d_X \text{ (kpc)} = 10^{0.2(DM_X - 10)}. \quad (28)$$

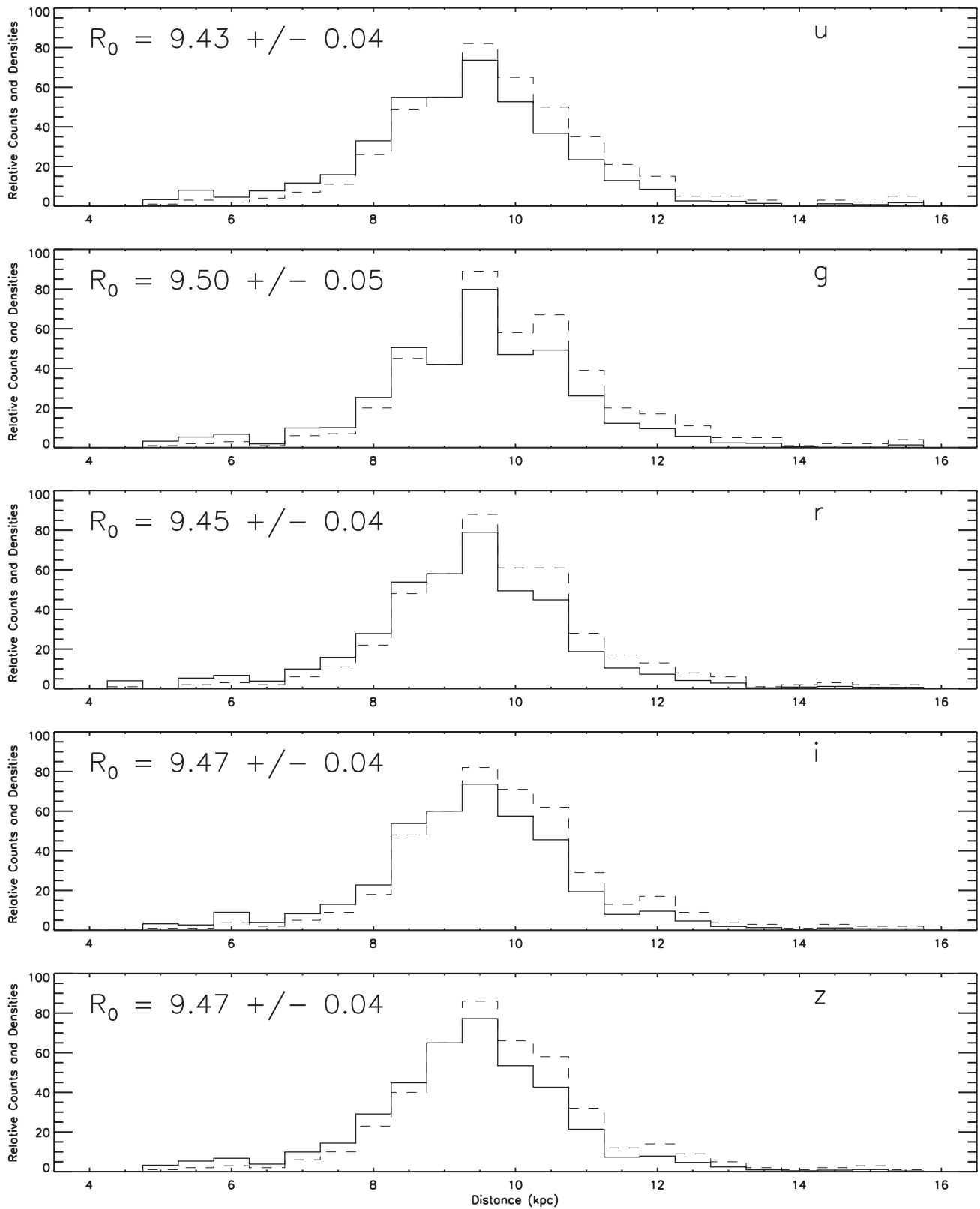


Figure 18. Distribution in distance of the RRab stars from Table 4 calculated from data in each of the five passbands and using the reddening law derived in this paper. The dashed lines show the histogram of star counts, while the bold line shows relative density by correcting for the larger sampled spatial volume at a larger distance, as was done for Figure 6. Contrary to what was seen in Figure 6, the results for the five passbands (labeled in the figure) are remarkably concordant, though surprisingly large compared with extant values of R_0 in the literature. Moreover, the density distribution with distance is sharply peaked, symmetrical, and very similar in all bands. This reinforces the need for the custom derivation of the reddening law for this line of sight provided in this work.

The distribution of d_x for the RRabs in Table 4 is shown in Figure 18 for each of the five bands using the dashed lines. The solid line shows the relative number density, in 0.5 kpc bins, by accounting for the change in the sampled volume with distance. For each band, the value of R_0 is determined by finding the location of maximum density, calculated as the “center of mass” from the five bins centered on the bin with the peak density. The results for the u , g , r , i , z bands (labeled in the figure) are remarkably concordant, though surprisingly large compared with extant values of R_0 in the literature. Moreover, the density distribution with distance is sharply peaked, symmetrical, and very similar in all bands. The quoted uncertainties reflect *only* the errors in finding the centroids in the histograms: systematic errors are discussed later separately. The mean of the u , g , r , i , z based results yields

$$R_0 = 9.47 \pm 0.04 \text{ kpc}, \quad (29)$$

where we do not reduce the uncertainties from the individual passband measurements because the departures from the respective centroids are highly correlated. Again the quoted uncertainty is only the random error estimated from the widths of the histogram peaks in Figure 18.

Our derived distance is at odds with the literature. A good compendium of determinations of R_0 up to 2015 is available from de Grijs & Bono (2016), including different kinds of tracers, statistical parallax methods, and analysis of the kinematics of stars near the Galactic nucleus. There are multiple reported values of R_0 from 7 to 9 kpc. After homogenization of the various determinations, they arrived at a statistical determination of $R_0 = 8.3 \pm 0.2(\text{statistical}) \pm 0.4(\text{systematic})$ kpc. By any account, our result presented here is about 10% higher than the norm.

The derived distances in each band depend on the $A_x/E(r-z)$ (slope) values in Equations (22)–(26). Note that while the derivation of these equations assumes a strong clumping of distances of the RRabs, it does not place any external constraint that the clump distance has to be identical across bands. That is, the intercepts in Equation (21) are determined independently from one band to another. There are several possible reasons why the derived value of R_0 here is larger than similar determinations from RR Lyrae stars in the past, but the three most pressing ones are as follows:

1. Our derived reddening is different from the standard reddening law, and as seen in Figure 8 predicts lower extinction in g , r , i , z than the standard reddening curve, making the corrected magnitudes fainter than what the standard law would give, thus resulting in a larger distance. Our result deserves some further scrutiny.
2. We have adopted the absolute magnitudes derived for the globular cluster M5 in Vivas et al. (2017) to apply also to the RR Lyrae in the Galactic bulge. If the RR Lyrae are different, for instance different Oosterhoff types, a distance discrepancy could result. We discuss this issue later.
3. The distance determination to M5, and hence the inferred absolute magnitudes of the RR Lyrae, may be incorrect.

We examine these possibilities in turn in some more detail. As mentioned previously, our finding in this paper is that the standard reddening law is violated in the direction of our field. For a given reddening, be it $E(r-z)$, $E(g-i)$, or even

$E(V-I)$, the extinction for all bands other than u is smaller with the reddening law derived here, compared to the standard formulation, as seen in Figure 8. Thus, for a given adopted absolute magnitude (in this case based on the adopted distance to M5), our reddening law yields larger distances compared to the standard law. This is clearly seen in the comparison of Figure 6 versus 18. Note specifically that in the i band, the standard law yields $R_0 = 8.04$ kpc from Figure 6, whereas Figure 18 using the reddening law derived here gives $R_0 = 9.47$ kpc. This 18% difference in distance is exactly explained by the difference in total to selective extinction for the i band given by Equation (17) versus Equation (22), given that the mean $E(r-z)$ in Field B1 is ~ 0.68 . The distances in all passbands when our derived reddening law is used are in agreement, whereas the use of the standard law produces disparate distances across the passbands. This validates the derivation of our reddening law through Equation (21). The departure from the standard reddening law in fields in the Galactic bulge has previously been reported by Nataf et al. (2016) and Nataf et al. (2013), who did a similar analysis with OGLE V , I and VISTA J , K_S photometry of RC giants.

The luminosity of RR Lyraes is less universal than the minimum light colors, and can depend on metallicity, post zero-age horizontal branch (ZAHB) evolution, and helium abundance. As remarked earlier, the average metallicity distribution of RR Lyrae stars in Baade’s window peaks at $[\text{Fe}/\text{H}] \approx -1.0$, as shown by Walker & Terndrup (1991; see their Figure 7). The metallicity of the globular cluster M5 is $[\text{Fe}/\text{H}] = -1.25 \pm 0.05$, according to Dias et al. (2016). This similarity notwithstanding, small differences in helium abundance can drive much larger differences in luminosity. A more robust test for differences can be had through the Period–Luminosity–Temperature (PLT) relation. Eddington’s pulsation equation $P\langle\rho\rangle^{1/2} = Q$ and its refinements (e.g., van Albada & Baker 1971), in combination with a mass–luminosity relation for any class of stars that share a common evolutionary state, implies the existence of a PLT relation for that stellar class. For RR Lyrae on the ZAHB, it means that stars with the same P and T should have the same luminosity L . This precept has been used to examine the cause of the Oosterhoff dichotomy (e.g., Sandage 1990, and references therein). Using the de-reddened mean color $(r-z)_0$ as a proxy for the effective temperature T , we compare the mean Period–Color relations for RRab in the globular cluster M5 and in our Field B1. The left-hand panel of Figure 19 shows that there is no net period shift at the same intrinsic color between M5 and the B1 field RRabs, thus implying that their luminosities are also at par. The average amplitude (the mean of amplitudes from all five bands, which is most robust against measurement errors) as a function of $\log P$ is shown on the right-hand panel: amplitudes have also been used in the literature as a proxy for temperature, but have been deprecated (Sandage 1990, and references therein). The left-hand plot is predicated on our determination of reddenings, while the right-hand one is reddening independent but its quality as a proxy for temperature is less secure. In both plots we see no indication of a difference between the RRabs in M5 versus those in the B1 field, which supports the contention that the luminosities are the same for the RRabs in both locations. Thus the second of the above possibilities is not a strong contender either.

This leaves us with the question of whether the calibration of absolute magnitudes through M5 could be in error. The

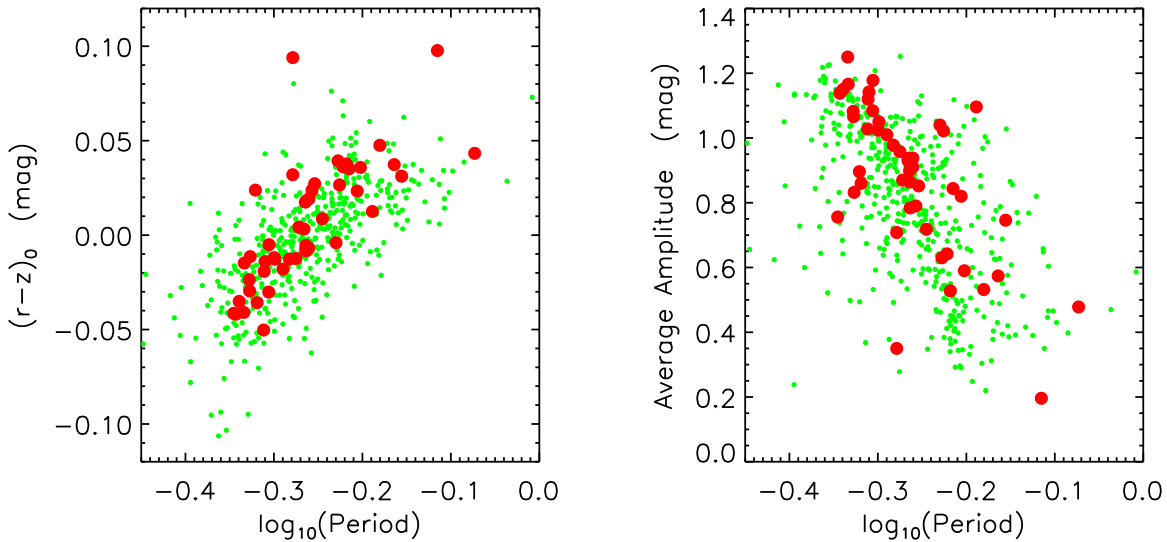


Figure 19. Comparison of the period–color and period amplitude relations for the RRabs in field B1 (green dots) and the globular cluster M5 (red filled circles). The agreement in the P-C and P-A distributions of both sets bolsters the assertion that the luminosity distributions of the RRabs for both instances are also the same, as argued in the text.

adopted distance modulus to M5, which is inherited from Vivas et al. (2017) through Equation (18), is based on main-sequence fitting. Layden et al. (2005) derived

$$\mu_0[\text{M5}] = 14.45 \pm 0.11. \quad (30)$$

Layden et al. (2005) also fitted the white dwarf sequence in M5 to the local white dwarfs with parallax distances, and obtained $\mu_0 = 14.67 \pm 0.18$, which is both more distant (which would make the RRabs brighter and R_0 even larger) and more uncertain. They report the average apparent V magnitude of ab-type RR Lyraes in M5 to be 15.025 ± 0.011 (from their Table 4). Correcting for extinction ($E(B - V) = 0.035$ and standard extinction law),

$$\langle m_V^0 \rangle[\text{M5RRab}] = 14.92 \pm 0.01, \quad (31)$$

which implies that the intrinsic V -band average absolute magnitude for RRab stars in M5 is

$$M_V^0[\text{M5RRab}] = 0.47 \pm 0.11. \quad (32)$$

A very recent determination of the distance to M5 by Gontcharov et al. (2019) gives $(m - M)_0 = 14.34 \pm 0.09$ by multi-band isochrone and main-sequence fitting, which, if adopted, would decrease R_0 to 9.04 kpc. In the *Gaia* era, we should look to astrometric measurements for a more definitive distance determination. From *HST* parallax measurements of field RR Lyrae stars, Benedict et al. (2011) obtain

$$M_V = 0.50 \pm 0.05 \quad (33)$$

for the M5 globular cluster metallicity of $[\text{Fe}/\text{H}] = -1.25$. This has a smaller formal uncertainty than Equation (32), while the 0.03 mag smaller distance modulus to M5 implied by the parallax-based RR Lyrae absolute magnitudes is within the uncertainties and yields

$$R_0 = 9.45 \pm 0.30 \text{ kpc}. \quad (34)$$

It is known that the *Gaia* DR2 results suffer from systematic errors in the measured parallax that vary with position in the sky, as discussed in Sections 4.2 and 4.3 of Arenou et al. (2018) and by Lindegren et al. (2018). The reported parallax of

0.1135 mas for M5 (Gaia Collaboration et al. 2018) is thus likely to be an underestimate by a few 10s of microarcsecs. It is expected that future *Gaia* data releases will ascertain and correct for this systematic error, but at the moment a direct distance to M5 based on published *Gaia* parallaxes is not reliable.

We can try instead to go through the *Gaia* DR2 parallax distances to calibrate the absolute magnitudes of RR Lyrae stars that are much closer to us than M5. Muraveva et al. (2018) present such an analysis for 401 RR Lyraes, which include objects that still are at distances of several kpc, and so suffer from systematic uncertainties mentioned previously. They also present a restricted sample of 23 RR Lyrae which have particularly well-determined metallicities, but this sample too is not made of solely the nearest objects, and thus is not free of the parallax systematics. From the results in their Table 4, which gives a linear correlation of M_V with $[\text{Fe}/\text{H}]$ that is consistent with an LMC distance modulus of 18.5, we read

$$M_V = (0.26^{+0.05}_{-0.05})[\text{Fe}/\text{H}] + 1.04^{+0.07}_{-0.07}. \quad (35)$$

Using $[\text{Fe}/\text{H}] = -1.25$ for the metallicity of M5 (Dias et al. 2016), we get

$$M_V = 0.72 \pm 0.07. \quad (36)$$

Combining Equations (31) and (36), we get a revised distance modulus to M5 of

$$\mu_0[\text{M5}] = 14.20 \pm 0.07. \quad (37)$$

This corresponds to a reduction of all distances by a factor of 0.89 ± 0.03 , implying that Equation (29) is changed to

$$R_0 = 8.44 \pm 0.28 \text{ kpc}, \quad (38)$$

which is consistent at the 1σ level with the recent determination of distance to the central black hole of 7.93 ± 0.13 kpc (Chu et al. 2018) and 8.13 ± 0.03 kpc (Abuter et al. 2018) from the analysis of the orbit of the star S2 around the central black hole.

The Muraveva et al. (2018) result includes data for the type-c RR Lyraes, which we have avoided in our analysis in the bulge. For this reason we have independently analyzed the data for the 41 type-ab RR Lyraes from the Muraveva et al. (2018)

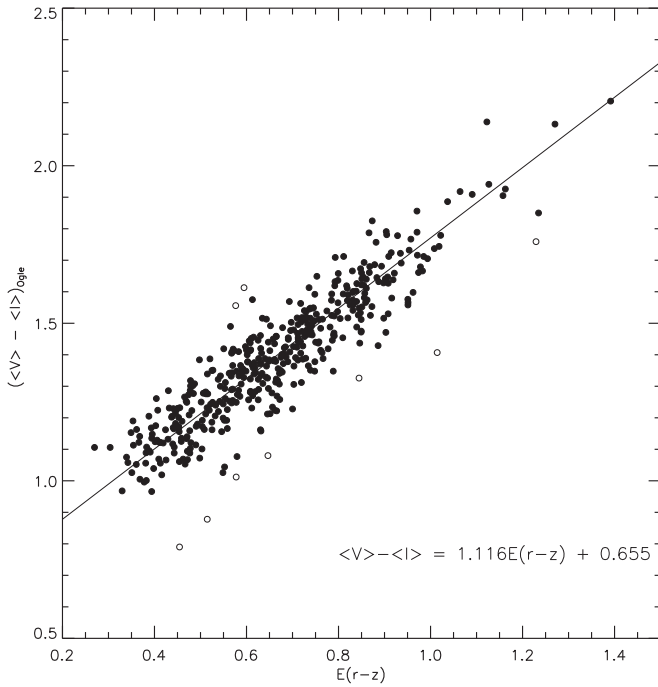


Figure 20. OGLE colors of individual RRabs cross-identified in Table 4 (from their mean magnitudes) are compared to their corresponding $E(r-z)$ values determined in this paper. A good correlation is seen. The scatter (0.08 mag in $\langle V \rangle - \langle I \rangle$) is much larger than the uncertainties in determining $E(r-z)$, which is a reflection of the fact that colors at minimum light are less variant from object to object than colors from mean magnitudes. The open circles indicate points that were rejected from the fit to a straight line.

sample that have *Gaia* DR2 parallaxes greater than 1 mas and so are least affected by the systematic uncertainties in the *Gaia* parallax zero point. Using the reported magnitudes and extinction estimates from their Table 1, we derive the equivalent of Equation (35) for this sample (rejecting the 3σ outlier AT And) to be

$$M_V \approx 0.35[\text{Fe}/\text{H}] + 1.06 \quad (\text{rms} = 0.13 \text{ mag}), \quad (39)$$

which yields $M_V \approx 0.62$ for the M5 RR Lyraes. This is brighter than the Muraveva et al. (2018) result, but significantly and definitely fainter than from Equation (32). As Muraveva et al. (2018) have pointed out, there are many selection effects to worry about from such ad hoc sample selection. The point of the exercise is to establish that there is enough uncertainty in the calibration of the RR Lyrae absolute magnitudes that 15% errors in distance determination are easily possible, and our derived value of $R_0 = 9.47$ kpc based on the Layden et al. (2005) main-sequence fitting distance to M5 awaits modification at a future time when the *Gaia* mission gives us a parallax distance to M5, or better yet, directly to the RR Lyrae (tracers of the oldest stars) in the bulge. For the present, we continue the discussion with our derived value in Equation (29) for the purpose of the remaining analyses of the structure of the bulge in this paper, noting that all quantitative distances will scale linearly with any change from $R_0 = 9.47$ kpc.

8.2. De-reddening and Distances to the OGLE RRabs

While determining minimum light colors for the bulge RRabs in the OGLE catalog is made difficult because of the paucity of *V*-band measurements, we examine the possibility of

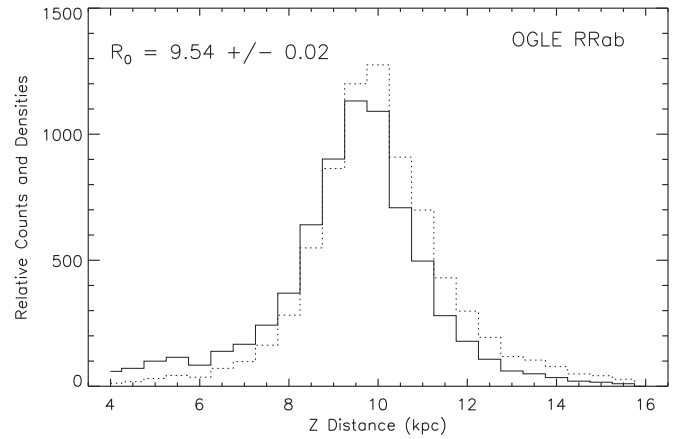


Figure 21. Histogram of star counts (dashed line) and RRab relative spatial density (solid line) as a function of projected distance along the direction toward the Galactic center. See text for details.

using their mean $\langle V \rangle$ and $\langle I \rangle$ magnitudes to estimate reddening to individual RRabs. We utilize the 472 RRabs in Table 4 for which we have cross-matches to the OGLE-III catalog, from which we obtain their $\langle V \rangle$ and $\langle I \rangle$ values, and relate them to our values for $E(r-z)$. This is shown in Figure 20. We derive the following relation

$$\langle V \rangle - \langle I \rangle = 1.116(\pm 0.027)E(r-z) + 0.655(\pm 0.018) \quad [\sigma = 0.08 \text{ mag}], \quad (40)$$

where σ indicates the rms scatter in $\langle V \rangle - \langle I \rangle$ for an individual RRab star. Compare the derived $\sigma \approx 0.08$ mag to the accuracy of better than 0.03 mag with which we can predict $E(g-i)$ from $E(r-z)$ using Equation (13): this is a consequence of using mean mags instead of colors at minimum light. A bivariate correlation of the extinction corrected mean $\langle i \rangle$ magnitudes (DECam system) derived in this paper to the observed $\langle V \rangle$ and $\langle I \rangle$ OGLE magnitudes of the corresponding RRabs yields the following relation:

$$\langle i \rangle_0 = 1.986 \langle I \rangle_{\text{OGLE}} - 1.031 \langle V \rangle_{\text{OGLE}} + 1.765 \quad [\sigma = 0.115 \text{ mag}], \quad (41)$$

which predicts the extinction corrected mean *i*-band magnitude (DECam system used in this paper) using the *observed* mean *V* and *I* OGLE magnitudes for any RRab star. The scatter indicates that the prediction is uncertain with an rms of 0.115 mag. Using this relation, we can get distances to individual RRab in the OGLE catalog with a 6% rms scatter (and additional systematic uncertainties from how well we know the absolute magnitudes of the RRabs).

Limiting ourselves to Galactic longitudes l bounded within $-5^\circ < l < +5^\circ$ and Galactic latitudes b within $-8^\circ < b < 0^\circ$ (where the line of sight looks relatively close to the Galactic center and the distances are not biased by RRabs in background star streams), we have 8092 RRabs from the OGLE-III catalog. Calculating their distances using Equations (41) and (32), we obtain the projected distance z on the scale of Layden's distance to M5 using Equation (27). We construct the histogram of the RRabs for z , as shown by the dashed lines in Figure 21. To make the histogram represent relative star densities, we reconstruct using a weighted count for each star, where the weight decreases as the inverse square of the line-of-

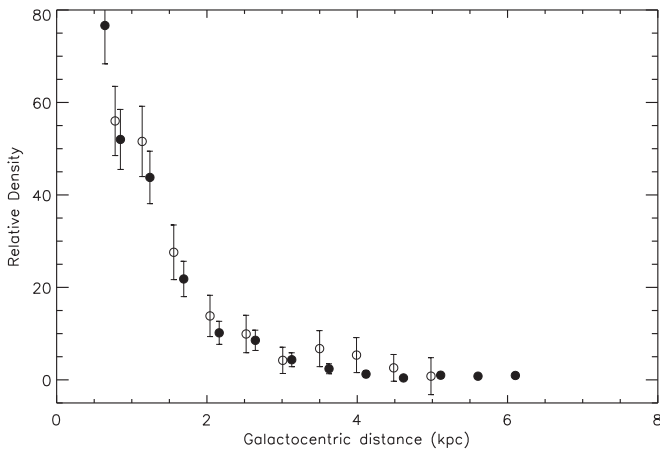


Figure 22. Relative density of RR Lyrae stars as a function of Galactocentric distance in kpc as derived from the RRabs in field B1. Open circles denote locations where the distance d from the Sun is less than R_0 , and filled circles for $d > R_0$. The error bars are calculated using Poisson statistics of the counts of RRab in each “bin.”

sight distance. The solid line in Figure 21 shows this modified histogram. Using the same peak centroiding methods as used previously, we obtain a peak density at $z = 9.54 \pm 0.02$ kpc, where the quoted uncertainty refers only to the centroiding error. If the spatial distribution of the RR Lyrae stars is azimuthally symmetric, z is a good estimator of R_0 . It differs from Equation (29) by less than 1%. On the one hand, this agreement is only to be expected, because the same precepts for reddening and absolute magnitudes of the RRabs have been used for both derivations. However, on the other hand, the sub-sample from OGLE-III used here has 40 times more stars, spread over a wider spatial extent, so the agreement validates implicit assumptions regarding the spatial distribution of the RR Lyraes. This result, however, is pre-mature in detail. Nataf et al. (2016) showed that not only is the reddening toward the bulge non-standard, but it also varies from one line of sight to another within the angular scale of the bulge. We might therefore expect that Equation (40), and therefore Equation (41) will be different for different lines of sight.

With the wider perspective of the OGLE coverage, it is now possible, in principle, by applying the reddening corrections as done here, to deduce the spatial distribution of the RR Lyraes near the Galactic center, especially the flattening of the density ellipsoid. The gaps in coverage in l and b , and possible incompleteness along lines of very high extinction, thwart the direct calculation of relative densities and make this task messy: we do not attempt it here. The caution mentioned above about variation of the reddening law itself along different sight lines also applies to most applications made possible by the OGLE RR Lyrae data set in the bulge. We will be able to ascertain how much Equations (40) and (41) change when we present the analysis for the five remaining fields in our study.

8.3. The Density Distribution of RR Lyraes in the Galactic Bulge

RR Lyrae are well-known tracers of ancient stellar populations. With more than 450 RRabs in our B1 field, whose line of sight passes close to the Galactic center, for which we have well derived distances, and from which we have derived a distance to the center R_0 , we are poised to examine the density distribution of the parent population of ancient stars. If the

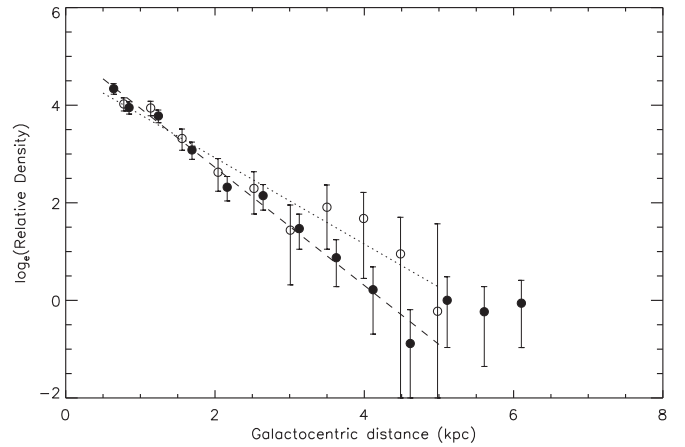


Figure 23. Natural log of the relative density of RR Lyrae stars as a function of Galactocentric distance in kpc as derived from the RRabs in field B1. Open circles denote locations where the distance d from the Sun is less than R_0 , and filled circles for $d > R_0$.

distance to an object is d , and its Galactic coordinates are l and b , then the Galactocentric distance r is given by

$$r^2 = R_0^2 + d^2 - 2dR_0 \cos(l)\cos(b). \quad (42)$$

Applying this to the count and density histograms derived in Section 8.1, and using $R_0 = 9.47$ kpc from Equation (29), we can remap them as a function of r . Figure 22 shows the distribution: open circles denote values for $d < R_0$ and filled circles for $d > R_0$. The error bars are calculated using Poisson statistics of the counts of RRab in each “bin,” and dividing by the normalized volume for the corresponding line-of-sight distance. Since the line of sight is at non-zero b , flattening of the bulge along the polar axis can produce different density values at the same r , for locations on the near side, versus those on the far side of the Galactic center.

Figure 23 shows the same plot, but now with the natural log of the relative density on the ordinate. The points out to $r < 5$ kpc appear to decrease linearly with r , indicating an exponential decline in the density of the form

$$\rho = Be^{-r/a}. \quad (43)$$

Formal fits to the near side (open circles) and far side (filled circles) show slightly different slopes of -0.90 and -1.21 kpc^{-1} , respectively, corresponding to $a = 1.11$ kpc and $a = 0.83$ kpc for the near and far sides, respectively. These (pseudo-)scale lengths obviously are along the line of sight and not along any axis of symmetry of the actual distribution (if indeed it is even elliptical). However, we expect to learn more from the other five fields in this study. On the far side there is a rise in the RR Lyrae density beyond $r \sim 5$ kpc. This may indicate an encounter of the line of sight with features in the thick disk (such as a spiral arm), or possibly a stellar stream. For instance, *Gaia* recently identified the remnant of a galaxy, Gaia-Enceladus, which merged with the Milky Way approximately 10 Gyr ago (Helmi et al. 2018). This merger produced different stellar streams that cover the entire sky and cross the Galactic disk, and also have associated RR Lyrae stars (see Figure 3 of Helmi et al. 2018).

9. Summary Discussion

To date, the bulge has been probed primarily by spectroscopy of the brighter stars (e.g., Kunder et al. 2011). We know

from this spectroscopy that there is a huge range of metallicities but no definitive constraints on the age distribution. The available giants do not proportionally represent all elements of the underlying population mix. Being mindful of the Initial Mass Function, one expects older stars to be over-represented among the giants, because their turnoff luminosities and masses are lower than their younger counterparts. Main-sequence stars in the bulge are prohibitively faint for detailed spectroscopic analysis, except when such stars are temporarily rendered brighter due to lensing events. From a handful of main-sequence stars studied in this way, Bensby et al. (2018) argue that there are significant numbers of stars younger than 8 Gyr in the central kilo-parsec, a conclusion that is apparently at odds with that from the study of giants alone. Given that the sample of 19 main-sequence stars is unlikely to increase significantly in the foreseeable future, it appears that the issue of selective representation of sub-populations of stars by the giants is best mitigated by the synthesis of observed Hess diagrams of the bulge, using methods along the lines of Dolphin (2002) that are capable of producing a more complete picture of the star formation history and the age–metallicity relation. Analyses of the VVV generated near-infrared CMDs are already underway (Surot et al. 2019). The visual wavelength multi-band CMDs presented here provide higher leverage on metallicities (and hence on ages as well), but they are not yet Hess diagrams where the selection effects and completeness are fully understood and characterized.

The production of adequate quality Hess diagrams of the bulge has faced several challenges. In this paper we have demonstrated that the major problem of decoding the line-of-sight reddening with sufficient angular resolution as well as deriving and applying the correct reddening law is tractable through the RR Lyrae stars. This builds on the work of Nataf et al. (2013, 2016), who used Red Giant Clump stars as standard candles and distance markers. Our work here uses independently derived photometry, a different color and distance marker, and extends the reddening analysis to much bluer passbands (where the clump shows structure in color). We have embarked on a program to search empirically for any systematic issues with RRab minimum light colors as a standard color marker, by extending the work done on the globular cluster M5 (Vivas et al. 2017), to a number of other RR Lyrae bearing clusters with different metallicities and Oosterhoff types. While the work presented here is thus a major step forward, there are two other issues that need resolving before the population synthesis mechanism can be brought to bear in full measure:

1. Removal of the foreground contamination along the line of sight. As discussed in Section 1, it is only a matter of time before surveys like VVV and their derivatives are able to solve this issue.
2. Estimation of the completeness in the CMDs. The usual procedure of deriving the completeness from artificial star tests is made more complicated by the extreme range and angular scales over which the extinction changes. Effectively, each 30 arcsec square bin must be evaluated independently. Extinction not only changes the de-reddened magnitude from the brightness recovered from the image, but also affects how crowded a given patch of the field appears, and the confusion limit for detection and measurement errors. This is not an intractable problem, but one that will be time-consuming. We intend

to address it after the equivalent of the study in this paper is done for all six of our fields.

So how might the CMDs generated here, and the equivalent for the other fields in our study, be used in the interim period before Hess diagrams with completeness estimates and foreground contamination removed can be produced? First, one can ascertain the locations of the stars that have been spectroscopically studied already on our CMDs. Are certain areas of the CMD excluded? A case in point are the more luminous among the “blue loop” stars discussed in Sections 6.4 and 6.5, and the associated questions raised by the existence of that feature. Are all regions of the fan-shaped giant branch structure in our CMDs represented? Have clump stars from different parts of the extended clump structure in Figure 11 been observed? How do stars from the blue and red ends of that extension differ in their spectroscopic characteristics? Conversely one can use the de-reddened CMDs to pick stars from regions of particular interest to follow up spectroscopically in the next generation of surveys, such as APOGEE V. When the equivalent CMDs for the other fields become available, we will be able to look for differences. Perhaps an empirical CMD of the foreground disk stars will emerge that will help model the foreground population in preparation for synthesizing the Hess diagrams to come. Our plan is to proceed first with deriving and presenting the CMDs for all the remaining fields, followed by work along the lines outlined previously.

We note that of the 4877 putative variables of all types we have detected, 2265 were detected independently in at least 2 of the 5 passbands, implying that these are almost certainly not false positives. Since our time coverage is limited and focused on obtaining light curves for RR Lyraes, our data are inadequate for obtaining light curves and periods for all these objects. Fortunately, many of these are also known and classified by the OGLE survey. Our five-band, de-reddened data for this set of objects are a “training set” for identifying variable stars from future LSST data, which will have sparse cadence, but information in panchromatic passbands. With the exception of the “Stripe 82” field from SDSS (e.g., Sesar et al. 2007; Bramich et al. 2008), there are no suitable publicly available data sets with time-domain coverage in multiple passbands at this time that are suitable for developing and testing algorithms for parsing variability characteristics from LSST data. Our results provide the ability for LSST time-domain brokering projects to develop the necessary techniques and algorithms to handle the variable star data that LSST will generate.





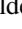
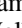
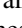
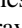

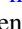




This project used data obtained with the Dark Energy Camera (DECam), which was constructed by the Dark Energy Survey (DES) collaboration. Funding for the DES Projects has been provided by the U.S. Department of Energy, the U.S. National Science Foundation, the Ministry of Science and Education of Spain, the Science and Technology Facilities Council of the United Kingdom, the Higher Education Funding Council for England, the National Center for Supercomputing Applications at the University of Illinois at Urbana-Champaign, the Kavli Institute of Cosmological Physics at the University of Chicago, the Center for Cosmology and Astro-Particle Physics at the Ohio State University, the Mitchell Institute for Fundamental Physics and Astronomy at Texas A&M University, Financiadora de Estudos e Projetos, Fundação Carlos Chagas Filho de Amparo à Pesquisa do Estado do Rio de

Janeiro, Conselho Nacional de Desenvolvimento Científico e Tecnológico and the Ministério da Ciência, Tecnologia e Inovação, the Deutsche Forschungsgemeinschaft, and the Collaborating Institutions in the Dark Energy Survey. The Collaborating Institutions are Argonne National Laboratory, the University of California at Santa Cruz, the University of Cambridge, Centro de Investigaciones Energéticas, Medioambientales y Tecnológicas-Madrid, the University of Chicago, University College London, the DES-Brazil Consortium, the University of Edinburgh, the Eidgenössische Technische Hochschule (ETH) Zürich, Fermi National Accelerator Laboratory, the University of Illinois at Urbana-Champaign, the Institut de Ciències de l'Espai (IEEC/CSIC), the Institut de Física d'Altes Energies, Lawrence Berkeley National Laboratory, the Ludwig-Maximilians Universität München and the associated Excellence Cluster Universe, the University of Michigan, the National Optical Astronomy Observatory, the University of Nottingham, the Ohio State University, the OzDES Membership Consortium the University of Pennsylvania, the University of Portsmouth, SLAC National Accelerator Laboratory, Stanford University, the University of Sussex, and Texas A&M University.

Based on observations at Cerro Tololo Inter-American Observatory, National Optical Astronomy Observatory (NOAO Prop. ID 2013A-0719; PI: A. Saha), which is operated by the Association of Universities for Research in Astronomy (AURA) under a cooperative agreement with the National Science Foundation.

We thank the support staff at CTIO for their excellent support during the observations. Olszewski was partially supported by NSF grants AST-1313001 and AST-1815767. We are grateful for the perceptive (and ultra-prompt) comments from an anonymous referee that have resulted in substantive improvements to the paper.

ORCID iDs

Abhijit Saha  <https://orcid.org/0000-0002-6839-4881>
 A. Katherina Vivas  <https://orcid.org/0000-0003-4341-6172>
 Knut Olsen  <https://orcid.org/0000-0002-7134-8296>
 Robert Blum  <https://orcid.org/0000-0002-8622-4237>
 Francisco Valdes  <https://orcid.org/0000-0001-5567-1301>
 Annalisa Calamida  <https://orcid.org/0000-0002-0882-7702>
 Alistair R. Walker  <https://orcid.org/0000-0002-7123-8943>
 Thomas Matheson  <https://orcid.org/0000-0001-6685-0479>
 Gautham Narayan  <https://orcid.org/0000-0001-6022-0484>
 T. Axelrod  <https://orcid.org/0000-0002-5722-7199>
 S. Bradley Cenko  <https://orcid.org/0000-0003-1673-970X>
 Andrea Kunder  <https://orcid.org/0000-0002-2808-1370>
 Adam Miller  <https://orcid.org/0000-0001-9515-478X>
 Stephen Ridgway  <https://orcid.org/0000-0003-2557-7132>

References

Abolfathi, B., Aguado, D. S., Aguilar, G., et al. 2018, *ApJS*, **235**, 42
 Abuter, R., Amorim, A., Anugu, N., et al. 2018, *A&A*, **615**, L15
 Arenou, F., Luri, X., Babusiaux, C., et al. 2018, *A&A*, **616**, A17
 Baade, W. 1946, *PASP*, **58**, 249
 Barbuy, B., Chiappini, C., & Gerhard, O. 2018, *ARA&A*, **56**, 223
 Benedict, G. F., McArthur, B. E., Feast, M. W., et al. 2011, *AJ*, **142**, 187

Bensby, T., Feltzing, S., Gould, A., et al. 2018, in IAU Symp. 334, *Rediscovering Our Galaxy*, ed. C. Chiappini et al. (Cambridge: Cambridge Univ. Press), 86
 Bernard, E. J., Schultheis, M., Di Matteo, P., et al. 2018, *MNRAS*, **477**, 3507
 Blanco, B. M. 1992, *AJ*, **103**, 1872
 Blanco, B. M., & Blanco, V. M. 1997, *AJ*, **114**, 2596
 Blum, R. D., Ramírez, S. V., Sellgren, K., & Olsen, K. 2003, *ApJ*, **597**, 323
 Bramich, D. M., Vidrih, S., Wyrzykowski, L., et al. 2008, *MNRAS*, **386**, 887
 Brown, T. M., Sahu, K., Zoccali, M., et al. 2009, *AJ*, **137**, 3172
 Burstein, D., & Heiles, C. 1978, *ApJ*, **225**, 40
 Calamida, A., Sahu, K. C., Anderson, J., et al. 2014, *ApJ*, **790**, 164
 Chu, D. S., Do, T., Hees, A., et al. 2018, *ApJ*, **854**, 12
 Clarkson, W., Sahu, K., Anderson, J., et al. 2008, *ApJ*, **684**, 1110
 Clement, C. M., Muzzin, A., Dufton, Q., et al. 2001, *AJ*, **122**, 2587
 de Grijs, R., & Bono, G. 2016, *ApJS*, **227**, 5
 Dias, B., Barbuy, B., Saviane, I., et al. 2016, *A&A*, **590**, A9
 Dolphin, A. E. 2002, *MNRAS*, **332**, 91
 Dwek, E., Arendt, R. G., Hauser, M. G., et al. 1995, *ApJ*, **445**, 716
 Fitzpatrick, E. L. 1999, *PASP*, **111**, 63
 Flaugher, B., Diehl, H. T., Honscheid, K., et al. 2015, *AJ*, **150**, 150
 Fukugita, M., Ichikawa, T., Gunn, J. E., et al. 1996, *AJ*, **111**, 1748
 Gaia Collaboration, Helmi, A., van Leeuwen, F., et al. 2018, *A&A*, **616**, A12
 García Pérez, A. E., Allende Prieto, C., Holtzman, J. A., et al. 2016, *AJ*, **151**, 144
 García Pérez, A. E., Ness, M., Robin, A. C., et al. 2018, *ApJ*, **852**, 91
 Gontcharov, G. A., Mosenkov, A. V., & Khovritchev, M. Y. 2019, *MNRAS*, **483**, 4949
 Helmi, A., Babusiaux, C., Koppelman, H. H., et al. 2018, *Natur*, **563**, 85
 Holtzman, J. A., Hasselquist, S., Shetrone, M., et al. 2018, *AJ*, **156**, 125
 Iben, I., Jr. 1964, *ApJ*, **140**, 1631
 Jönsson, H., Allende Prieto, C., Holtzman, J. A., et al. 2018, *AJ*, **156**, 126
 Kiraga, M., Paczyński, B., & Stanek, K. Z. 1997, *ApJ*, **485**, 611
 Kormendy, J., & Kennicutt, R. C., Jr. 2004, *ARA&A*, **42**, 603
 Kunder, A. M., de Propris, R., Rich, M., et al. 2011, AAS Meeting, **217**, 241.12
 Layden, A. C., Sarajedini, A., von Hippel, T., & Cool, A. M. 2005, *ApJ*, **632**, 266
 Lindegren, L., Hernández, J., Bombrun, A., et al. 2018, *A&A*, **616**, A2
 Majewski, S. R., Schiavon, R. P., Frinchaboy, P. M., et al. 2017, *AJ*, **154**, 94
 Martig, M., Fouesneau, M., Rix, H.-W., et al. 2016, *MNRAS*, **456**, 3655
 Minniti, D., Dékány, I., Majaess, D., et al. 2017, *AJ*, **153**, 179
 Minniti, D., Lucas, P. W., Emerson, J. P., et al. 2010, *NewA*, **15**, 433
 Muraveva, T., Delgado, H. E., Clementini, G., Sarro, L. M., & Garofalo, A. 2018, *MNRAS*, **481**, 1195
 Narayan, G., Axelrod, T., Holberg, J. B., et al. 2016, *ApJ*, **822**, 67
 Nataf, D. M., Gonzalez, O. A., Casagrande, L., et al. 2016, *MNRAS*, **456**, 2692
 Nataf, D. M., Gould, A., Fouqué, P., et al. 2013, *ApJ*, **769**, 88
 O'Donnell, J. E. 1994, *ApJ*, **422**, 158
 Pietrukowicz, P., Udalski, A., Soszyński, I., et al. 2012, *ApJ*, **750**, 169
 Pinsonneault, M. H., Elsworth, Y., Epstein, C., et al. 2014, *ApJS*, **215**, 19
 Saha, A., & Hoessel, J. G. 1990, *AJ*, **99**, 97
 Saha, A., Olszewski, E. W., Brondel, B., et al. 2010, *AJ*, **140**, 1719
 Saha, A., & Vivas, A. K. 2017, *AJ*, **154**, 231
 Sandage, A. 1990, *ApJ*, **350**, 631
 Schechter, P. L., Mateo, M., & Saha, A. 1993, *PASP*, **105**, 1342
 Schlegel, D. J., Finkbeiner, D. P., & Davis, M. 1998, *ApJ*, **500**, 525
 Schultheis, M., Rojas-Arriagada, A., García Pérez, A. E., et al. 2017, *A&A*, **600**, A14
 Sesar, B., Ivezić, Ž., Grammer, S. H., et al. 2010, *ApJ*, **708**, 717
 Sesar, B., Ivezić, Ž., Lupton, R. H., et al. 2007, *AJ*, **134**, 2236
 Skottfelt, J., Bramich, D. M., Figuera Jaimés, R., et al. 2015, *A&A*, **573**, A103
 Soszyński, I., Udalski, A., Szymański, M. K., et al. 2014, *AcA*, **64**, 177
 Stanek, K. Z. 1996, *ApJL*, **460**, L37
 Sturch, C. 1966, *ApJ*, **143**, 774
 Surot, F., Valenti, E., Hidalgo, S. L., et al. 2019, *A&A*, in press (arXiv:1902.01695)
 Valdes, F., Gruendl, R. & DES Project 2014, in ASP Conf. Ser. 485, *Astronomical Data Analysis Software and Systems XXIII*, ed. N. Manset & P. Forshay (San Francisco, CA: ASP), 379
 van Albada, T. S., & Baker, N. 1971, *ApJ*, **169**, 311
 Vivas, A. K., Saha, A., Olsen, K., et al. 2017, *AJ*, **154**, 85
 Walker, A. R., & Terndrup, D. M. 1991, *ApJ*, **378**, 119
 Zasowski, G., Schultheis, M., Hasselquist, S., et al. 2019, *ApJ*, **870**, 138